

AD-A244 382



2

NPS-PH-92-004

NAVAL POSTGRADUATE SCHOOL

Monterey, California



DTIC
ELECTE
JAN 16 1992
S B D

LOMPOC VALLEY DIFFUSION EXPERIMENT ANALYSIS -
MT. IRON COMPARISON AND TWO ZONE CONVECTIVE
SCALING MODEL

C. E. SKUPNIEWICZ

R. F. KAMADA

AND S. A. DRAKE

JANUARY 1992

technical report

92-01232



Approved for public release; distribution unlimited

Prepared for:
USAF Space Division, SSD/CLGR
Los Angeles, CA 90009-2960

92-01232

Naval Postgraduate School
Monterey, California


Rear Admiral R. W. West, Jr.
Superintendent

H. Shull
Provost

This report was prepared for and funded by the U.S. Air Force Space Systems Division.


Reproduction of all or part of this report is authorized.

This report was prepared by:


C. E. SKUPNIEWICZ
Meteorologist

Reviewed by:

Released by:


KARLHEINZ E. WOEHLE
Chairman, Department of Physics


PAUL J. MARTO
Dean of Research

UNCLASSIFIED
SECURITY CLASSIFICATION OF THIS PAGE

REPORT DOCUMENTATION PAGE				Form Approved OMB No. 0704-0188	
1a REPORT SECURITY CLASSIFICATION UNCLASSIFIED			1b RESTRICTIVE MARKINGS		
2a SECURITY CLASSIFICATION AUTHORITY			3 DISTRIBUTION AVAILABILITY OF REPORT approved for public release; distribution unlimited		
2b DECLASSIFICATION/DOWNGRADING SCHEDULE					
4 PERFORMING ORGANIZATION REPORT NUMBER(S) NPS-PH-92-004			5 MONITORING ORGANIZATION REPORT NUMBER(S)		
6a NAME OF PERFORMING ORGANIZATION Naval Postgraduate School		6b OFFICE SYMBOL (If applicable) PH		7a NAME OF MONITORING ORGANIZATION Aerospace Corp., Chemical Systems	
6c ADDRESS (City, State, and ZIP Code) Monterey, CA 93943-5000			7b ADDRESS (City, State, and ZIP Code) Los Angeles, CA 90009		
8a NAME OF FUNDING SPONSORING ORGANIZATION USAF Space Division		8b OFFICE SYMBOL (If applicable) SSD/CLGR		9 PROGRAM ELEMENT IDENTIFICATION NUMBER MPIR FY7616890425	
8c ADDRESS (City, State, and ZIP Code) Los Angeles, CA 90009-2960			10 SOURCE OF FUNDING NUMBERS		
			PROGRAM ELEMENT NO	PROJECT NO	TASK NO
			WORK UNIT ACCESSION NO		
11 TITLE (Include Security Classification) Lompoc Valley Diffusion Experiment Analysis - Mt. Iron Comparison and Two Zone Convective Scaling Model (unclassified)					
12 PERSONAL AUTHOR(S) C. E. Skupniewicz, R. F. Kamada and S. A. Drake					
13a TYPE OF REPORT technical		13b TIME COVERED FROM 10/90 TO 9/92		14 DATE OF REPORT (Year, Month, Day) 920102	
15 PAGE COUNT 110					
16 SUPPLEMENTARY NOTES					
17 COSATI CODES			18 SUBJECT TERMS (Continue on reverse if necessary and identify by block number)		
FIELD	GROUP	SUB-GROUP			
			Atmospheric Diffusion, plume dispersion, Vandenberg AFB, Lompoc, convective scaling, stratocumulus		
19 ABSTRACT (Continue on reverse if necessary and identify by block number) The results of the Lompoc Valley Diffusion Experiment (LVDE), conducted at Vandenberg AFB, California in 1989, are compared to the predictive equations of the Mt. Iron Diffusion Tests, conducted at Vandenberg in the 1960's. The Mt. Iron equation parameterizes diffusion with on-base meteorological tower input data. Regression techniques similar to those of Mt. Iron are employed in this comparison, resulting in LVDE equations which use the same meteorological data as input. Instantaneous and time averaged center-line concentrations, in both flat and complex terrain are analyzed. For all cases LVDE concentrations are shown to decrease with range less rapidly than the Mt. Iron equation predicts. This cannot be attributed to differing experimental designs. We suggest that this bias is due to gravitational and/or scavenging losses of the tracer material used in Mt. Iron. A "two zone" convective scaling equation is developed which diffuses the plume differently in cloud covered and clear sky portions of the domain. The method is shown to be superior to homogeneous convective scaling equations, and comparable to a (cont'd)					
20 DISTRIBUTION AVAILABILITY OF ABSTRACT <input checked="" type="checkbox"/> UNCLASSIFIED/UNLIMITED <input type="checkbox"/> SAME AS RPT <input type="checkbox"/> DTIC USERS			21 ABSTRACT SECURITY CLASSIFICATION UNCLASSIFIED		
22a NAME OF RESPONSIBLE INDIVIDUAL C. E. Skupniewicz			22b TELEPHONE (Include Area Code) (408) 646-2451		22c OFFICE SYMBOL PH

DD Form 1473, JUN 86

Previous editions are obsolete
S/N 0102-LF-014-6603

SECURITY CLASSIFICATION OF THIS PAGE
UNCLASSIFIED

UNCLASSIFIED

SECURITY CLASSIFICATION OF THIS PAGE

19. statistical approach based on the plume measurements. While the method works for maximum concentration predictions, it fails for plume width and cross wind integrated concentration for $X > 6$. We speculate that this is due to near-surface topographic flows which spread the plume at the surface but maintain centerline concentration.

UNCLASSIFIED

SECURITY CLASSIFICATION OF THIS PAGE

INDEX

1. Introduction	3
2. Background	4
3. Mt. Iron Regression Analysis Methodology	6
4. Mt. Iron Regression Results	12
5. Conclusions and Recommended Regression Equations	39
6. Basic Equations	40
7. The Convective Scaling Approach	42
8. Convective Scaling Applied to LVDE	54
9. Two Zone Convective Scaling	61
10. Convective Scaling Model Comparison - General	67
11. Convective Scaling Model Comparison - Statistics	80
12. Comparison of Regression & Convective Scaling Results	84
13. Conclusions and Recommended Convective Scaling Equations (C_0/Q)	87
14. Recommended Convective Scaling Equations (σ_y, C_y)	90
15. Recommended Instrumentation Upgrades and Future Work	91
Appendix A - Convective Scaling Velocity	92
Appendix B - Plume Centerline and Cloud Edge Determination	102
References	109

Accession For	
NTIS GRA&I	<input checked="" type="checkbox"/>
DTIC TAB	<input type="checkbox"/>
Unannounced	<input type="checkbox"/>
Justification	
By _____	
Distribution/	
Availability Codes	
Dist	Avail and/or Special
A-1	



LOMPOC VALLEY DIFFUSION EXPERIMENT ANALYSIS -
MT. IRON COMPARISON AND TWO ZONE CONVECTIVE SCALING MODEL

2 January 1992

C.E. Skupniewicz, R.F. Kamada, and S.A. Drake

Environmental Physics Group
Naval Postgraduate School
Monterey, California 93943-5000
DSN 878-2451
Commercial (408)-646-2451

1. Introduction

This document presents results from the Lompoc Valley Diffusion Experiment (LVDE), completing tasks related to the LVDE data analysis described in contract number MPIRF7616890425 funded by USAF HQ Space Systems Division, Los Angeles (SSD/CLGR). This report uses data sets described in the LVDE Data Report (Skupniewicz et al. 1991a), and therefore detailed descriptions of the measurements and methods of LVDE are not supplied herein. The LVDE Data Report also supplies some basic analyses of the data, such as plume trajectories, regional wind flow patterns, and synoptic descriptions.

The first objective of this analysis is to compare LVDE results to the Mt. Iron equations, and to formulate new expressions specific to LVDE. During this procedure, we simulate the methods used in the Mt. Iron reports (Hinds and Nickola 1968). We discuss differences in the results, and show some difficulties with the statistical approaches used in the Mt. Iron analysis. The second objective is to compare LVDE data to theories developed for diffusion of passive materials from surface sources in convective conditions. We extend those basic theories to accommodate the added complexities of the LVDE domain.

2. Background

For those readers without access to the LVDE Data or Mt. Iron reports, we describe these experiments briefly in this section. LVDE was conducted during August 1989 to assess the potential risk of gaseous releases from the Hypergolic Stockpile and Storage Facility (HSSF) at Vandenberg AFB, California. Previous studies of wind flow patterns and hypothetical gaseous releases showed that trajectories could pass over populated areas near Lompoc, California during typical daytime onshore wind flow (Kamada et al. 1989). Thus, tests were conducted under normal daytime "sea breeze" conditions. Releases were near-surface (12 ft) and continuous. The trace gas was SF_6 with downwind sampling by mobile electron-capture gaseous samplers. The instrumented vehicles travelled

roads which intersected the plume at 2-15 km ranges. LVDE also included a series of releases from within the adjacent Lompoc Valley 2 km north of the HSSF. We term these "flat terrain" data as opposed to the hilly complex terrain downwind of the HSSF.

The Mountain Iron Diffusion Tests² were a series of surface releases conducted in the 1960's from Space Launch Complexes 4 and 6 (SLC4,6). The original report developed a range of regression-based equations, depending upon the release site of interest and the input measurements available. This report uses a concentration vs. range equation developed for SLC4 which is 2 miles south of the HSSF. Terrain downwind of SLC4 is similar in complexity to the HSSF downwind terrain. The releases were typically 30 minutes in duration. The trace material was a fluorescent aerosol (zinc sulfide, GMD 2.5 microns). Downwind sampling was accomplished with vacuum samplers distributed along available roads on the base. The results from Mt. Iron are presently used for assessment of neutral gas surface spills from locations in this general area.

While LVDE and Mt. Iron were conducted under similar wind flow patterns and the release locations were within 4 km of each other, some fundamental differences in the experimental designs are noted here. First, Mt. Iron released tracer for relatively short periods of time, typically 30 minutes, while the LVDE release durations of four to seven hours were essentially continuous (when compared to the travel time of the plume to sample locations). Secondly, the

Mt. Iron trace material was collected over the duration of the release, giving a dosage, or time integrated concentration, while LVDE data were gathered from rapid transects through the plume giving "instantaneous" crosswind concentration profiles. Plume parameters calculated from the LVDE data can be modeled with two-particle statistical theory, useful in estimating the crosswind growth of instantaneous releases ("puffs"). When time-averaged, the LVDE data simulates the growth of continuous plumes, described by single-particle diffusion theories. The time-averaged form of the LVDE data is more comparable to the Mt. Iron results than the instantaneous data.

3. Mt Iron Regression Analysis Methodology

Risk assessments of most types of gaseous releases at Vandenberg are primarily concerned with the hourly averaged surface-level maximum concentration. The concentration is integrated over the time of exposure, resulting in accumulated dosage. The USAF Surgeon General has set maximum dosage levels for various gases based on toxicology studies and standards set by other public health organizations (e.g. OSHA).

A primary goal of Mt. Iron was to predict centerline concentration using measurements from meteorological towers located at or near the release sites. The tower data is readily available

at Vandenberg in near real time. Investigators chose a multi-parameter regressive approach, assuming that

$$\frac{C_m}{Q} = f(x, \sigma_\theta, \Delta T, U) = a_1 x^{a_2} \sigma_\theta^{a_3} \Delta T^{a_4} U^{a_5} \quad , \quad (1)$$

where C_m is maximum ground-level concentration, Q is release rate, x is downwind range, σ_θ is standard deviation of the wind direction, ΔT is temperature difference between tower sensors at 54 ft and 6 ft, and U is wind speed. The left hand side of the relationship is dimensioned (ppm NO_2 -min)/lb. Concentrations of any other chemical species are obtained by multiplying the expression by the ratio of their molecular weights to that of NO_2 . From the right hand side uses the non-conventional units: ft, degrees, deg F, and knots. While these units are awkward by present standards, we retain this convention to compare LVDE with Mt. Iron directly. The Mt. Iron experiment did not measure concentrations, but rather dosage accumulated over the period of release. Results were later converted to concentration by assuming uniform concentration over the release period, and dividing by the release period and sampler flow rate.

The regression parameters used in Mt. Iron were chosen for their significance to the physics of diffusion. Turbulence intensity, i.e. σ_θ , is of primary importance. The spectral

characteristics of turbulence determine changes in diffusion as a function of plume travel time, and this can often be related to atmospheric stability, e.g. the bulk Richardson number,

$$Ri_b = \frac{gz^2}{T} \left(\frac{\frac{\partial T}{\partial z} + \gamma_d}{U^2} \right) , \quad (2)$$

therefore, ΔT and U were chosen as regression parameters. The centerline concentration is also a function of the plume material, release rate, distance from the source, and possibly other meteorological or physical quantities.

It is apparent that several of the regression parameters are interdependent. This implies that multivariate regression equations formed by combinations of these variables may not be unique. Therefore, it makes more physical sense to group the parameters in non-dimensional forms, thus reducing the number of empirically derived constants. We also note that the Mt. Iron regression neglects some important physical quantities, e.g., the mixing depth, h . We will discuss these issues further in following sections.

The original technique for evaluating the Mt. Iron equations was to count the number of occurrences of samples which fell within factors of two and four of the equation predictions. While other grading schemes may be more insightful, we have kept this "factor

grade" approach for comparison. We have also evaluated the results by using the normalized mean-squared-error (NMSE) and fractional bias (FB), measures favored by other investigators (e.g. Hanna and Strimatis (1991)). These are defined as

$$NMSE = \frac{\overline{(C_p - C_o)^2}}{\overline{C_o} \overline{C_p}} \quad , \quad (3)$$

and

$$FB = 2 \frac{\overline{C_o} - \overline{C_p}}{\overline{C_o} + \overline{C_p}} \quad , \quad (4)$$

where subscript o refers to the observations and p refers to the equation predictions. By dividing by the mean observed and predicted values, NMSE tends to give equal weight to under-predictions and over-predictions. For example, in the case of two observations of say, 5.0, then a prediction of 2.5 has the same NMSE as a prediction of 10.0. In a similar manner, FB gives the percent of over or under-prediction. Both measures suffer from the problem that the error characteristics cannot be a function of the absolute value of the data. I.e., the NMSE or FB at 1 ppm should be the same as that at 1 ppb. If not, the data at 1 ppm will be given more weight. We found concentration independence to be true for our application of NMSE, but untrue for FB applications. Therefore we define an alternative measure, "geometric" fractional

bias,

$$GFB = \frac{\log (C_o/C_p)}{\text{abs} (\log (C_o/C_p))} \quad (5)$$

which is similar to FB but with a logarithmic weighting. GFB at low concentrations are equivalenced with bias at higher absolute concentration. The disadvantage of GFB is that it cannot be directly related to a fraction of over or under-prediction.

Mt. Iron results are given both in terms of median value and "95% confidence" equations. We are unclear as to how the original investigators derived the 95% confidence equations, but the two forms are related by a simple fraction, i.e., only parameter a_1 in eq. 1 differs between the two equations. We obtain a 95% confidence equation by assuming a normal distribution with a variance of NMSE. Then approximating 95% confidence at "two sigma",

$$\frac{C_m}{Q} (95\%) = (1 + 2 \sqrt{NMSE}) \frac{C_m}{Q} (50\%) \quad (6)$$

Unfortunately, base communications to the meteorological tower

at the release site (WT057) failed just prior to the start of LVDE. While we were able to capture some data by interfacing to the outgoing 1 minute data stream, these data are not processed through the base computer system into the standard 10 minute averages and have numerous data gaps. Rather than deciphering and simulating the processing, and deleting data during the met data lapses, we decided to use a nearby tower (WT054) for the met inputs. The tower chosen was about 1 mile from the release site, roughly the same distance from the coast, in similar terrain with respect to surface roughness, and under similar cloud cover as during the releases. Met data from two other towers were also tried in the analysis (WT058 and WT300).

In Skupniewicz et al. (1991a), we calculated the centerline maximum concentration via three methods. The "moment" method performs moment statistics on the cross-wind concentration distributions. The other two methods assume a Gaussian crosswind profile. The "maximum" method assumes that the maximum observed concentration is true, then forces σ_y to agree with the cross-wind integrated concentration (CWIC). The last method is based solely on CWIC, forcing both the maximum and σ_y to conform to the shape of the profile. We use only the "maximum" method for these regressions, since we want the most direct measure of maximum centerline concentration.

Hourly averages were calculated with the following equations;

$$\sigma_y = \sqrt{\frac{\sum_{i=1}^N \sigma_{y,i} C_{m,i} (y_i^2 + \sigma_{y,i}^2)}{\sum_{i=1}^N \sigma_{y,i} C_{m,i}} - \left(\frac{\sum_{i=1}^N \sigma_{y,i} C_{m,i} y_i}{\sum_{i=1}^N \sigma_{y,i} C_{m,i}} \right)^2} \quad (7)$$

$$C_m = \frac{\sum_{i=1}^N \int C dy}{\sqrt{2\pi} \sigma_y} \quad (8)$$

where subscript i denotes instantaneous transects and y_i is the cross-wind position of the instantaneous maximum concentration.

4. Mt. Iron Regression Results

Figures 1-4 compare the range dependence of the LVDE data to that of Mt. Iron for both instantaneous and time averaged, and both flat and complex terrain data sets. The following generalities apply to all figures:

* Any data points overlaid with "star" symbols were edited prior to the regression analysis, but were included in the grading schemes.

* Unless otherwise indicated, the Mt. Iron equation is the 95% confidence version (operationally used at Vandenberg), while the LVDE data are median (50%) values. The Mt. Iron 95% line is approximately a factor of 3 higher than the Mt. Iron median line. We directly compare 95% values later in the report.

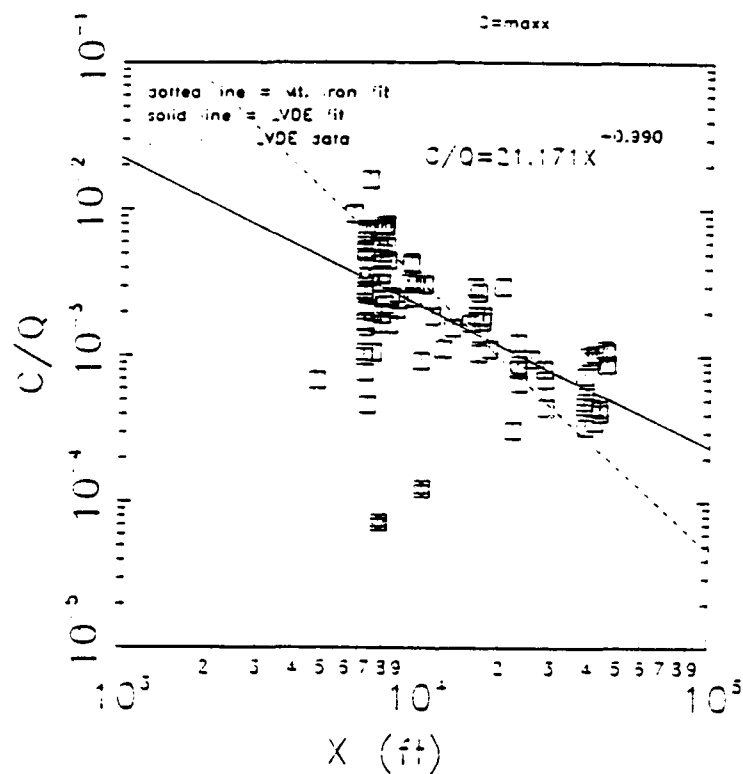


Figure 1. Instantaneous maximum concentrations normalized by the release rate vs. downwind distance for the HSSF release site.

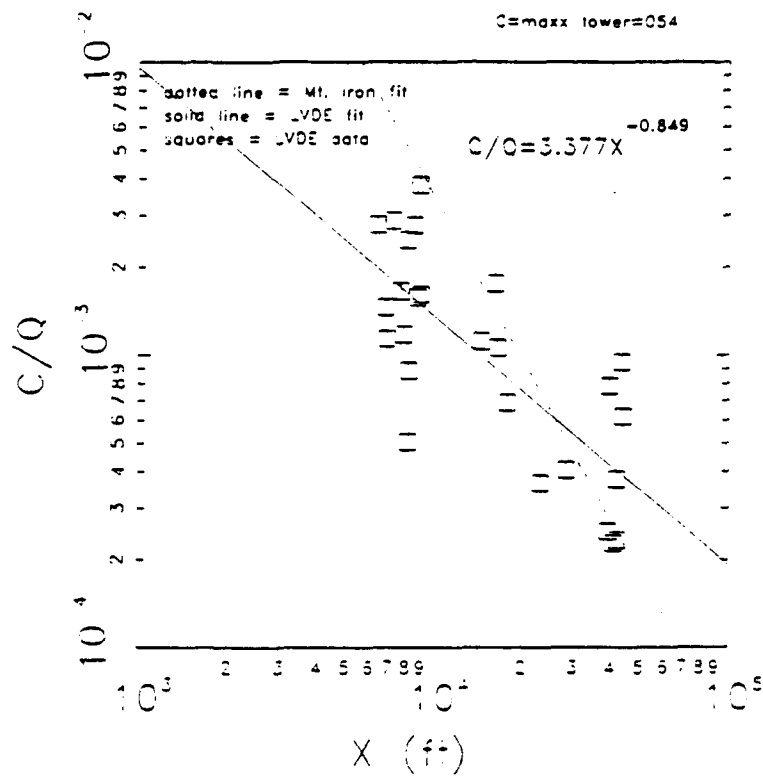


Figure 2. One hour averaged maximum concentrations normalized by the release rate vs. downwind distance for the HSSF release site.

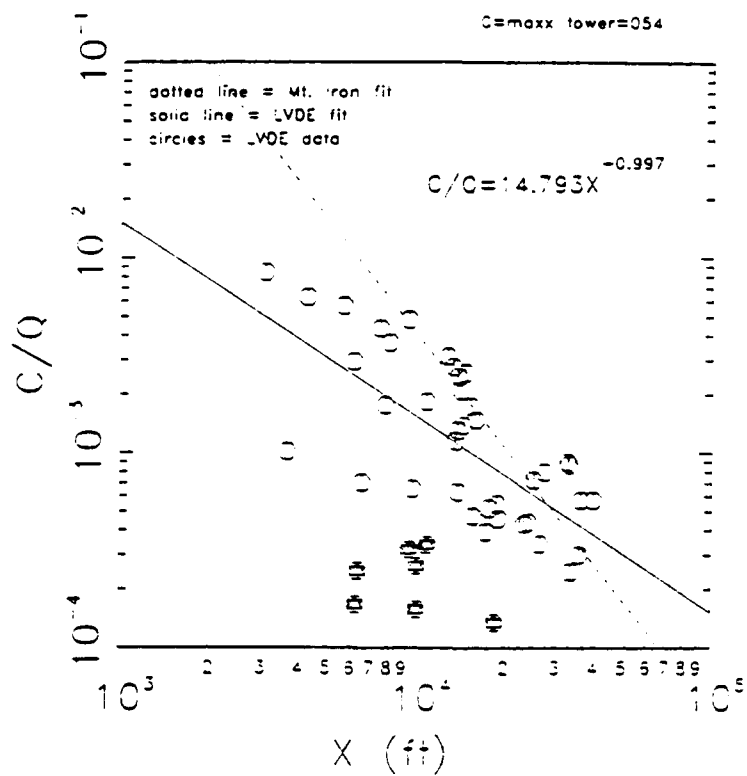


Figure 3. Instantaneous maximum concentrations normalized by the release rate vs. downwind distance for the Lompoc Valley release site.

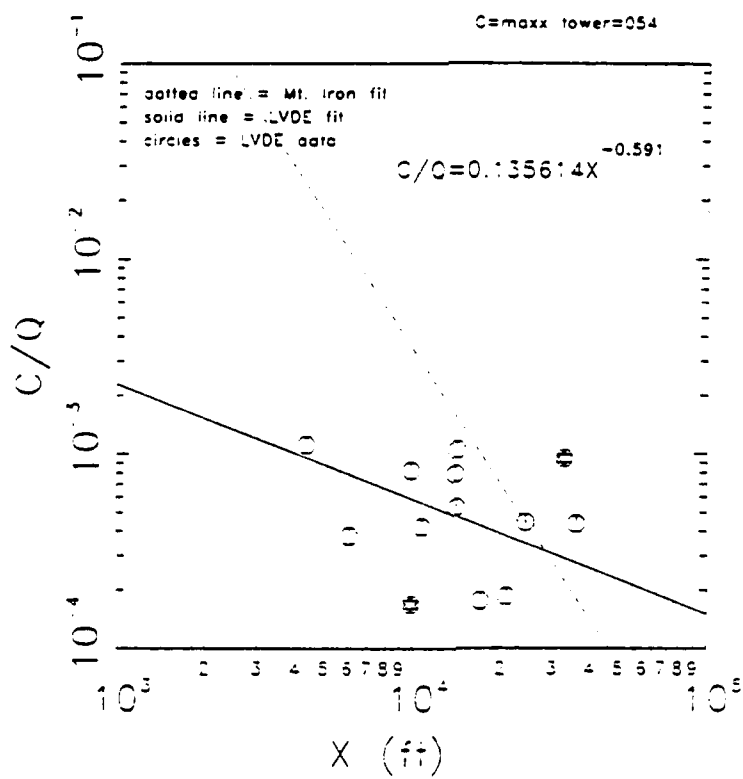


Figure 4. One hour averaged maximum concentrations normalized by the release rate vs. downwind distance for the Lompoc Valley release site.

For ranges where plume dimensions are small compared to the dominant turbulence scale, theory predicts that concentrations resulting from a puff (instantaneous data) would drop less rapidly with range than plume concentrations (time averaged data). We see this effect by comparing the instantaneous data of figs. 1-3 to the time averaged results of figs. 2-4. Equations obtained from curvilinear range dependent fits to the LVDE data are at the top of each figure. The exponents in the regression equations indicate the rate of concentration decrease with range. Comparing the instantaneous to time averaged exponents, we see smaller exponential decreases after averaging is applied.

In all cases, the best fit through the LVDE data is less sloped than the line obtained by regressing the Mt. Iron equation against the downwind distance. This shows that the Mt. Iron concentrations decrease much more rapidly with range than the LVDE data. This feature cannot be attributed to the "short" Mt. Iron release time (30 min). The short releases of Mt. Iron should cause the data to behave in a more "plume-like" fashion at short ranges and more "puff-like" at long range, resulting in a greater slope than a true continuous release would show. This is not observed. Several factors could produce these differences. A fall-out of Mt. Iron tracer material with increasing range would produce this effect. Enhanced diffusion at short range (compared to Mt. Iron), or decreased diffusion at long range could also produce these

results. Unfortunately, regression techniques such as these do not allow for a unique diagnosis of these differences.

Figures 5-8 apply a multi-variate curvilinear regression to the full set of parameters listed in eq. 1, and plot that solution against the measurements. The data scatter within the factor two and four lines is very similar to the Mt. Iron results; 73% of the Mt. Iron data were within a factor of two of the predictions and 97% were within a factor 4. The NMSE values are quite small compared to other model evaluations such as Hanna and Strimatis (1991), but this is misleading because our regression results are being tested against the data from which they were obtained. The improvements in the factor grades and NMSE after averaging are also somewhat artificial because the number of data points has been reduced, and the data sets are not independent. If we employ the central limit theorem, assuming samples from the same normally distributed population, we would expect roughly a factor of 3.7 reduction in the variance for both the HSSF and Lompoc Valley averaging processes. If we take the ratio of the NMSE values, we find reductions of 2.4 for HSSF releases and 2.1 for the Lompoc Valley releases, well below the central limit for both cases. This shows that the averaging process has actually added some variance to the data.

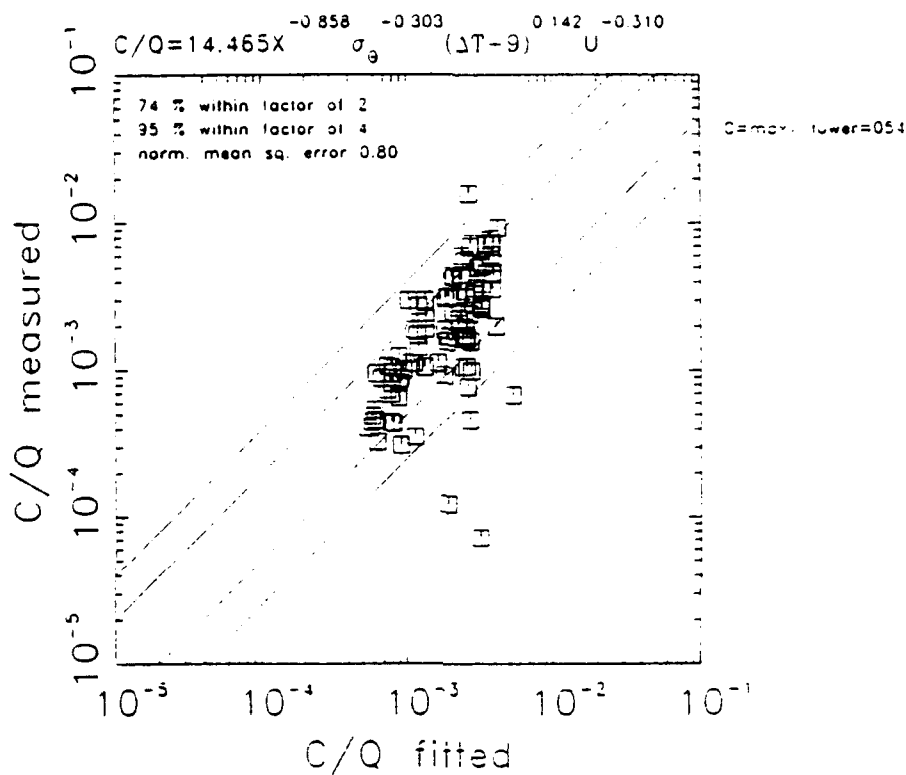


Figure 5. Scatter plot of instantaneous observed concentrations vs. multi-parameter regression equation (listed at top) for HSSF releases. Diagonal lines represent values within a factor of two and four of agreement. No data have been edited when calculating these "goodness of fit" grades.

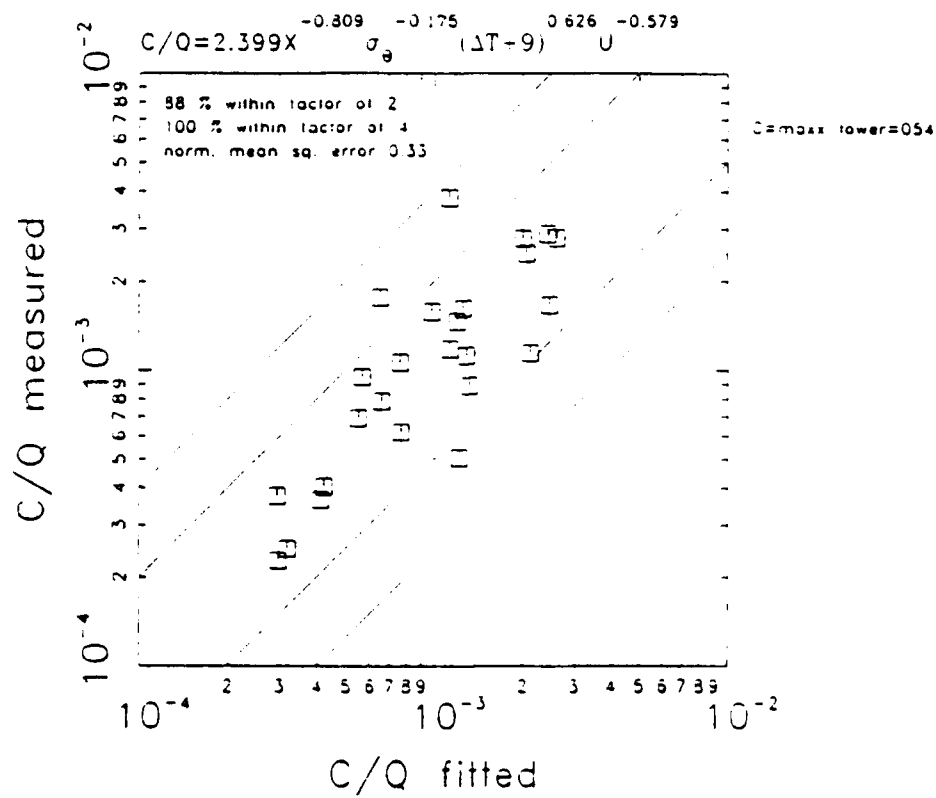


Figure 6. Same as figure 5, except data are one hour averaged concentrations from HSSF releases.

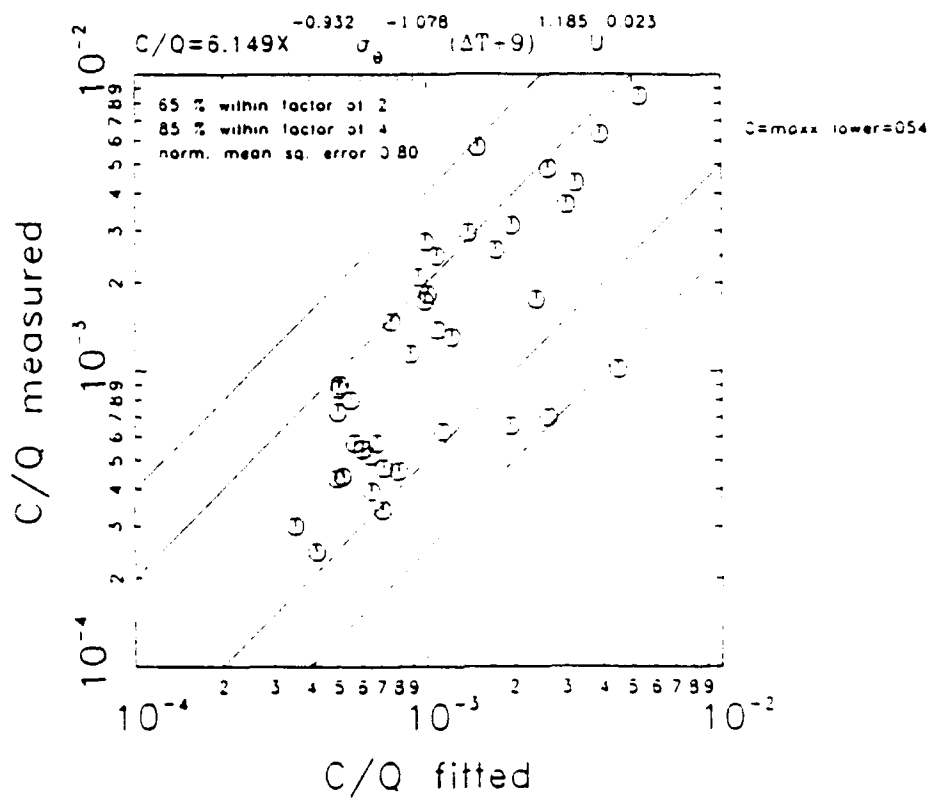


Figure 7. Same as figure 5, except data are instantaneous concentrations from Lompoc Valley releases.

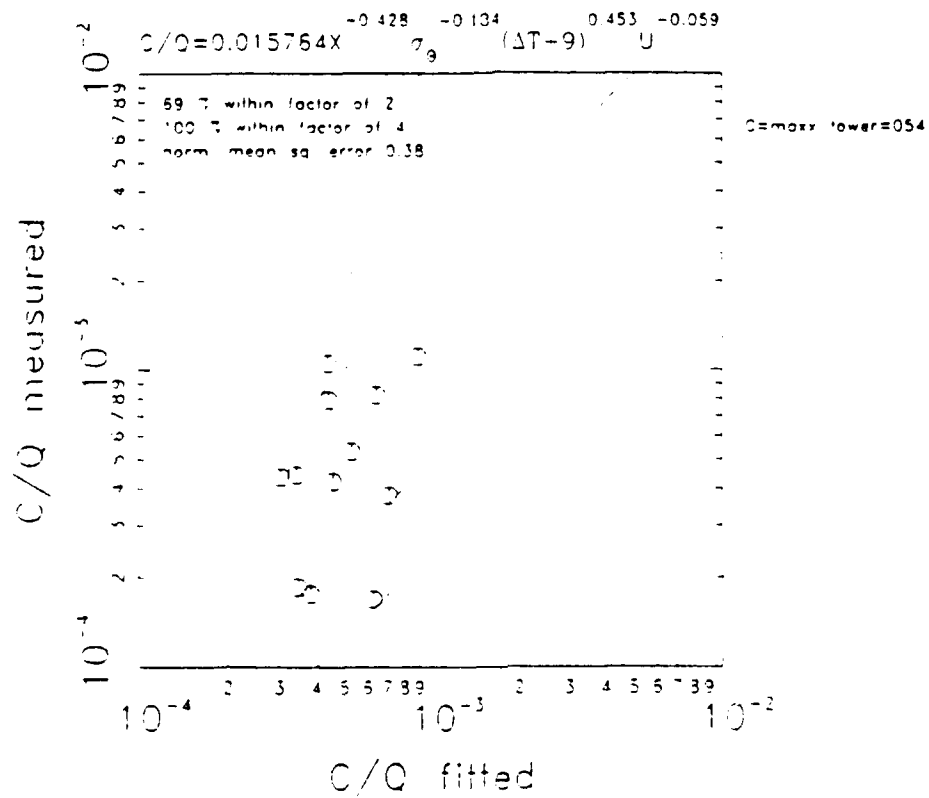


Figure 8. Same as figure 5, except data are time averaged concentrations from Lompoc Valley releases.

We next discuss concentration dependence on σ_θ , ΔT , and U as measured at the local met tower. The most disturbing feature of the σ_θ regressions were weak C/Q correlations with measured turbulence for the HSSF release site (e.g., fig. 9). We would expect a well defined negative relationship between C/Q and σ_θ , since higher turbulence disperses the cloud more rapidly. The negative correlation is better for Lompoc valley releases (fig. 10), but the scatter is large. The poor correlation is contrary to most theoretical descriptions of dispersion, and probably indicates a flaw in the measurement system. We have determined that the base computer system does simple averaging of one minute σ_θ values to determine longer averages. This high pass filtering incorrectly eliminates much of the turbulence responsible for diffusing the plume. Steps are under way to correct this situation at the base.

When we applied a multi-variate curvilinear fit to the range and σ_θ parameters, we obtained only a minimal improvement in the factor grades and NMSE over the range fits alone. This small degree of increased predictability is largely due to the lack of C/Q correlation with σ_θ . Therefore, the exponent for σ_θ in figs. 5-8 are poor estimates, and can suggest a stronger relationship than truly exists (e.g. fig. 7). Indeed, the Mt. Iron exponent may be just as unreliable as the LVDE exponents, but without the original data, we cannot confirm this hypothesis.

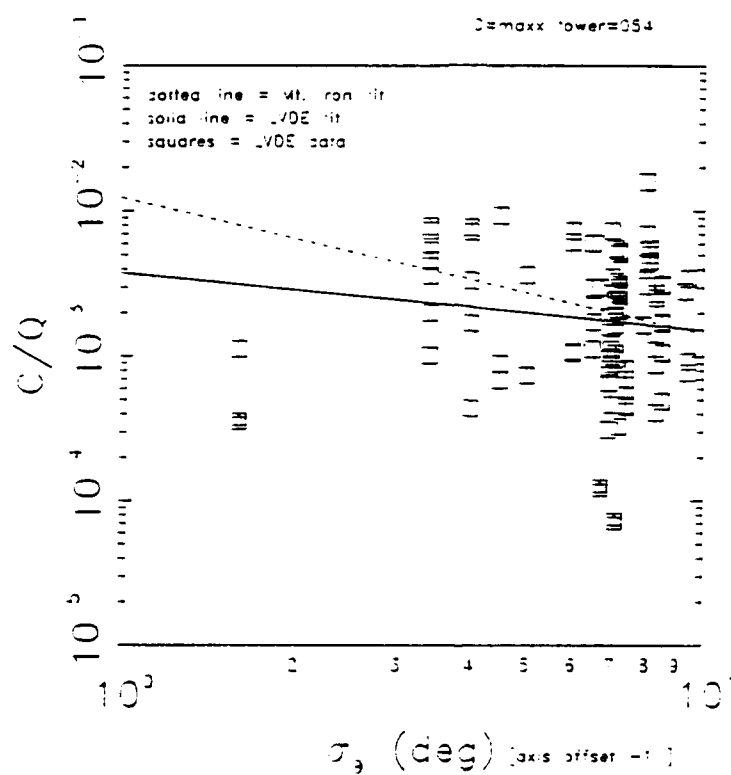


Figure 9. Instantaneous maximum concentrations normalized by the release rate vs. turbulence (σ_θ) for the HSSF release site.

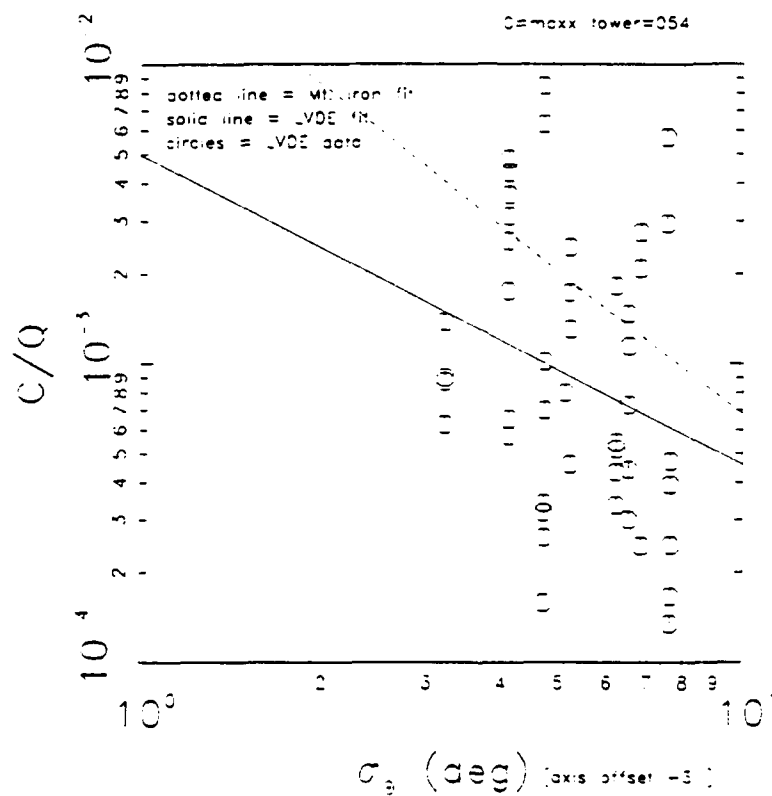


Figure 10. Instantaneous maximum concentrations normalized by the release rate vs. turbulence (σ_θ) for the Lompoc Valley releases.

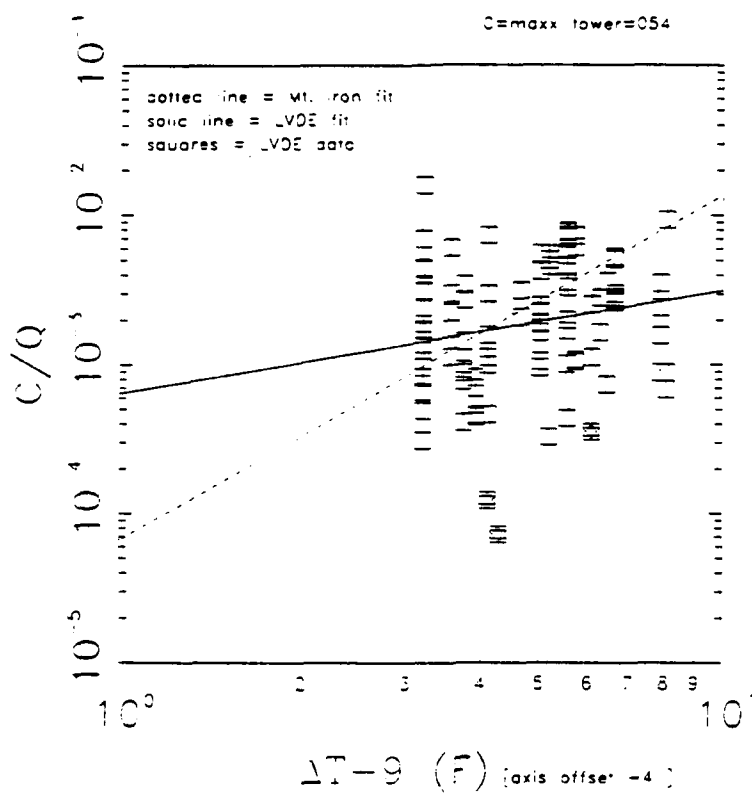


Figure 11. Instantaneous maximum concentrations normalized by the release rate vs. vertical temperature difference at tower 054 for the HSSF release site.

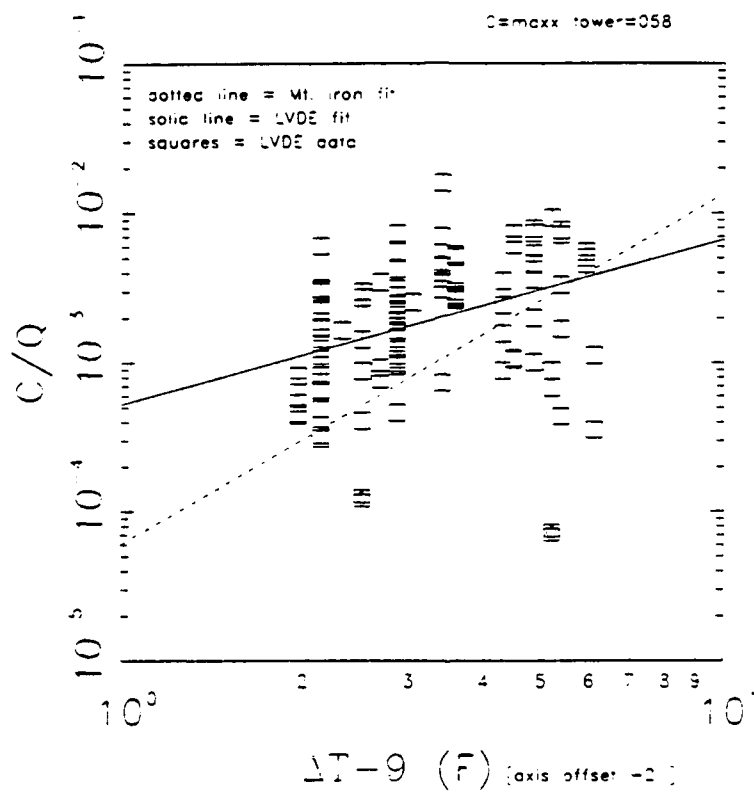


Figure 12. Instantaneous maximum concentrations normalized by the release rate vs. vertical temperature difference at tower 058 for the HSSF release site.

The temperature difference between 54 ft and 6 ft is a rough measure of atmospheric stability; more negative values indicate more convection and therefore greater dispersion. As in the original Mt. Iron reports, our analyses add 9 deg F to ΔT in order to stabilize the regression by keeping values positive. We expect a positive relationship with ΔT . We found this to be true, but again, the scatter is large. The dependence is weak for WT054 data (fig. 11) because it was mainly under the clouds where stability is near neutral. The same data plotted against WT058 temperature differences (fig. 12) showed significantly better correlation, especially for low (more negative) temperature differences. ΔT is generally smaller at WT058 because it was mainly in clear skies and unstable conditions. Performing the multiple variable regression reflects this dependence, with significant error reductions for WT058 met data compared to WT054 data. A subtle conclusion may be made from this exercise. In some cases, the release site tower may not be the best choice for calculating dispersion. For releases under cloud cover, the release site would most likely be in nearly neutral conditions. However, the dispersion along the plume pathway takes place primarily in clear skies. Thus, better correlation may be observed for ΔT 's measured in the clear skies, as was the case with WT054 and WT058.

Wind speed is a natural dispersion parameter for a continuous

plume because the amount of material released into a unit volume of air (for a constant mass release rate) decreases linearly with wind speed. When we regress concentration against wind speed alone, we find a strong negative relationship for all towers (figs. 13-14). However, when we included wind speed in a multi-variate regression with the other parameters, we did not observe a significant error reduction. This is reflected in the wide variation of exponents given in figs. 5-8. We attribute this paradox to interdependencies between regression parameters. For example, the lower effective release rate with increasing wind speed is compensated to some degree by lower turbulence intensity values, and therefore less dispersion.

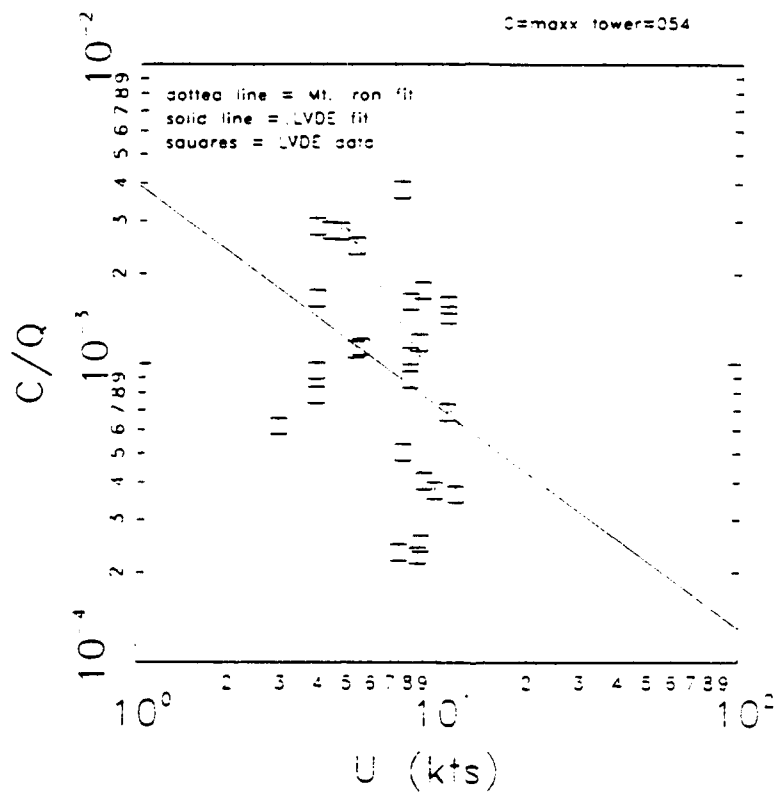


Figure 13. One hour averaged maximum concentrations normalized by the release rate vs. wind speed for the HSSF releases.

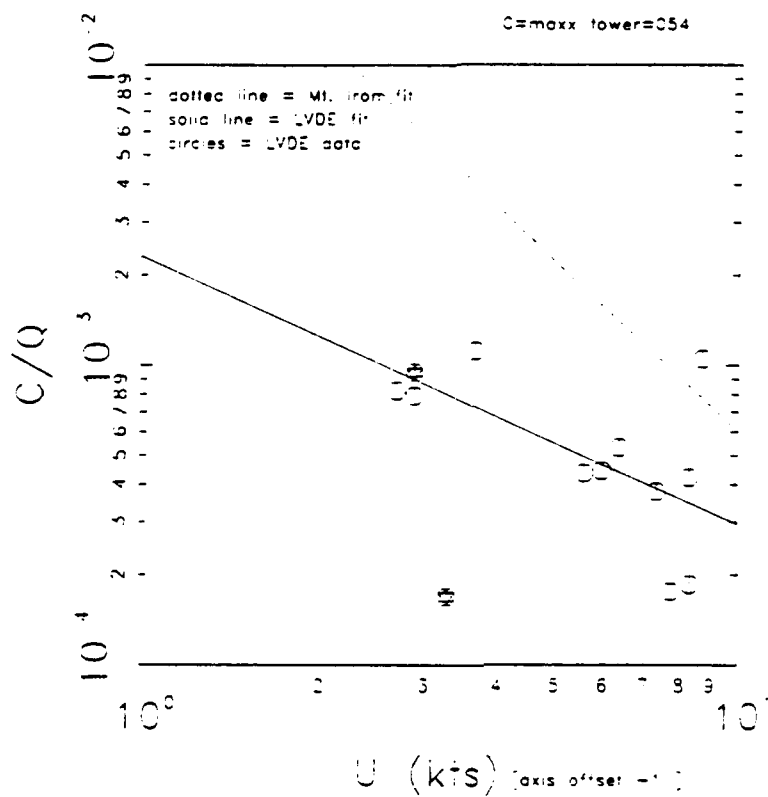


Figure 14. One hour averaged maximum concentrations normalized by the release rate vs. wind speed for the Lompoc Valley releases.

Figures 15-18 apply eqn. 6 to the LVDE data, giving 95% confidence figures. The recommended 95% confidence equation for time averaged HSSF releases is given atop fig. 16. These figures show, in an absolute sense, the difference between the measurements. For all cases we see a bias change with concentration. Figure 16, the case which should agree most closely, shows significantly larger LVDE values than Mt. Iron concentrations at low absolute values (longer ranges). The bias is reduced or eliminated at higher concentrations (shorter ranges). Again, this changing bias could be explained by a fall-out of Mt. Iron tracer material with increasing range, enhanced diffusion at short range (compared to Mt. Iron), or decreased diffusion at long range. Unfortunately, we cannot deduce the cause from these regression analyses.

Figure 16 demonstrates that GFB may be more appropriate than FB in those cases in which the bias changes with concentration. The large negative fractional bias occurs because a few high-valued "predictions" (Mt. Iron) are greater than the "observations" (C/Q measured), when in reality the observations are generally larger. The geometric fractional bias is close to negligible, since the higher LVDE values for lower concentrations are given equal weight.

Inspection of figs. 16 and 18 also indicates that the time averaged "flat terrain" concentrations are generally lower than the

"complex terrain" data, while figs. 15 and 17 show negligible difference for the instantaneous data. Comparing the HSSF and Lompoc Valley releases for distance only regression (figs. 1-4), we see that the flat and complex terrain data are similar in an instantaneous sense, but the flat terrain concentrations (Lompoc Valley) decrease less rapidly in a time averaged sense. The large scatter and small number of data points leave us wary of suggesting physical processes for these differences. However, we further analyze Lompoc Valley - HSSF differences later in this report.

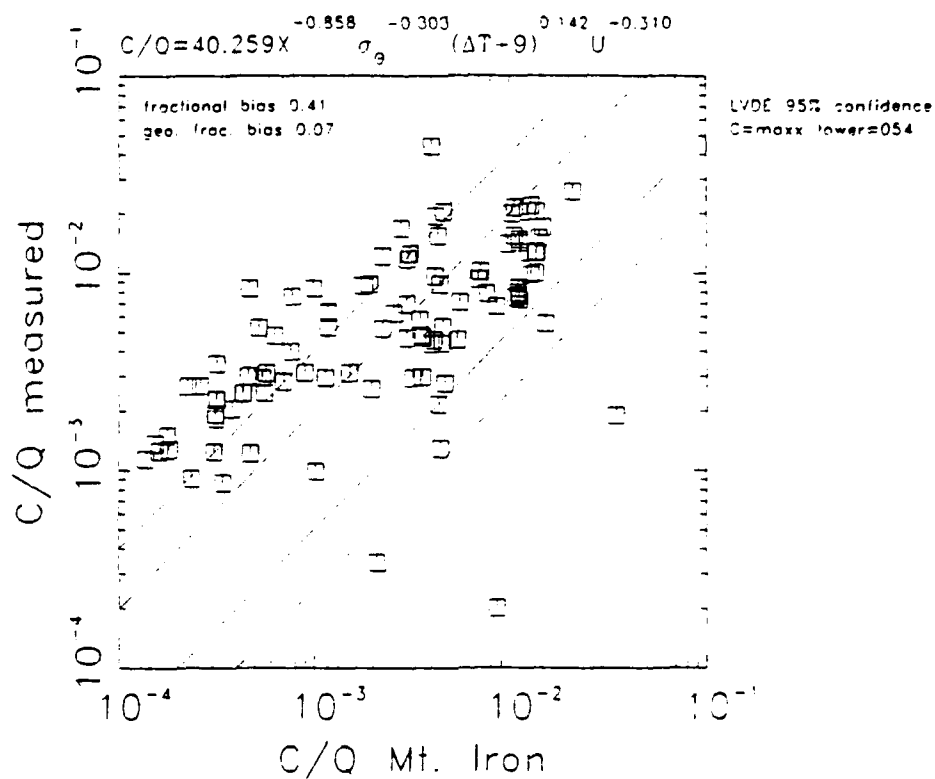


Figure 15. Scatter plot of instantaneous observed concentrations vs. the Mt. Iron multi-parameter regression equation for HSSF releases. Data have been adjusted to "95% confidence" and the corresponding LVDE regression equation is listed at the top. Diagonal lines represent values within a factor of two and four of agreement. No data have been edited when calculating these "goodness of fit" grades.

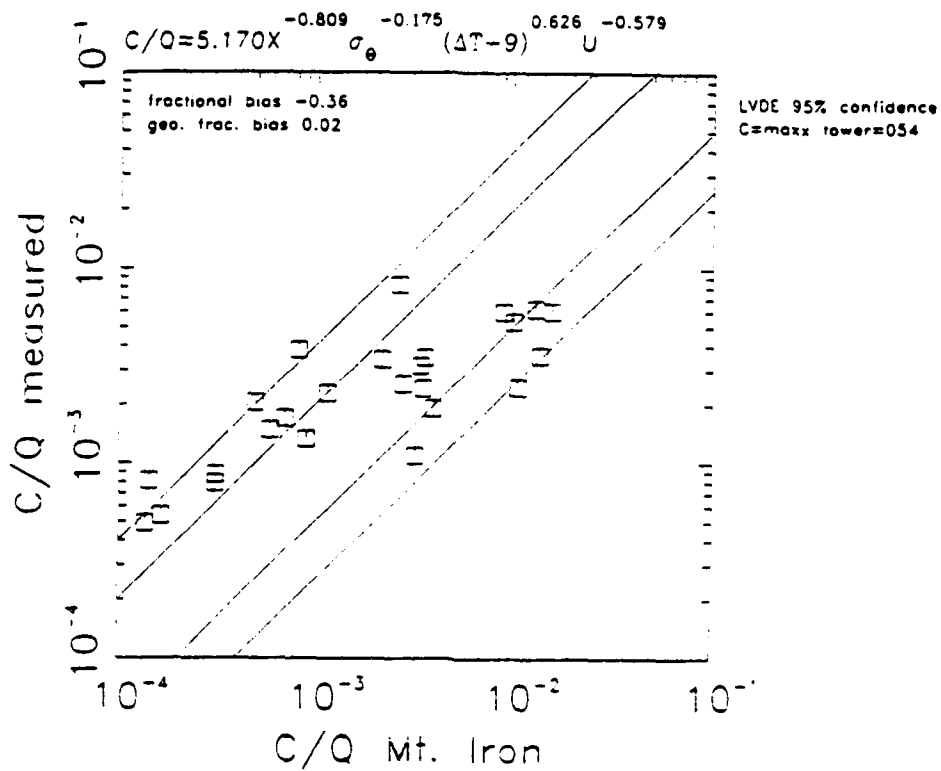


Figure 16. Same as figure 15, except data are time averaged concentrations from HSSF releases.

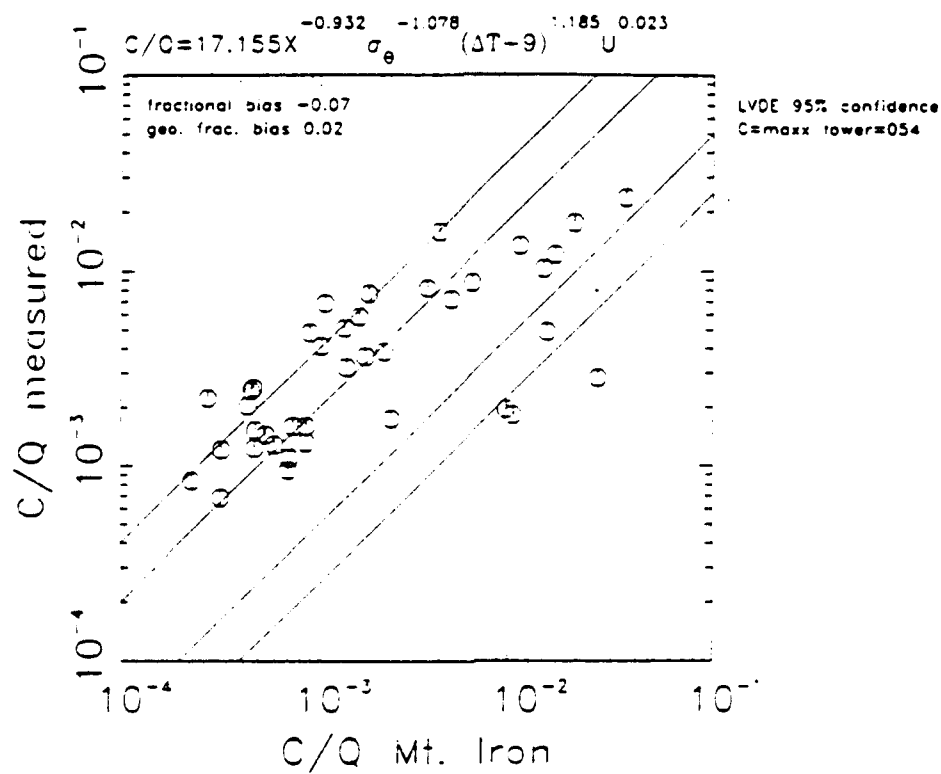


Figure 17. Same as figure 15, except data are instantaneous concentrations from Lompoc Valley releases.

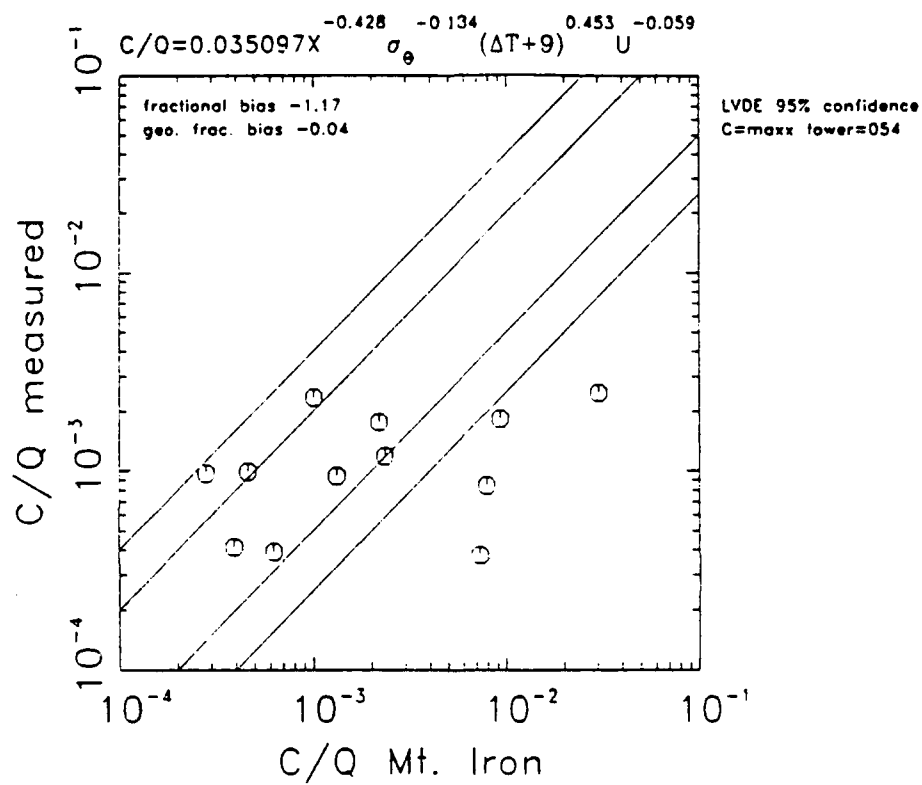


Figure 18. Same as figure 15, except data are time averaged concentrations from Lompoc Valley releases.

5. Conclusions and Recommended Regression Equations

We observe significant differences between the LVDE data and the Mt. Iron equations, mainly in the low dose range where the Mt. Iron values are lower than those observed in LVDE. We speculate but cannot confirm that these differences may stem from losses of the zinc sulfide aerosol used in Mt. Iron due to gravitationally settling and impact with uneven terrain. Significant improvement in the regression predictions are not obtained by adding turbulence or wind speed to the set of regression parameters. The short (1 minute) time of averaging may be responsible for the low correlation with turbulence. Correlation of wind speed with other regression parameters (e.g. ΔT) most likely negates improvement in the regression's concentration predictions. Regression predictions for the HSSF release site are significantly different from those for Lompoc Valley releases.

Because of these ambiguities, we recommend validation, verification and certification of a more physically based diffusion model for cold spill modeling at Vandenberg. If a verified regression algorithm must be used in the interim, we recommend the equation given in fig. 16 for predictions of hourly averaged concentrations resulting from continuous releases at the HSSF, and the equation in fig. 1. for instantaneous concentrations. LVDE measurements were made along trajectories between the HSSF and

Lompoc or Miguelito Canyon and only during daylight hours. Therefore, we only recommend the use of our regression results for flows in this general direction and for non-stable boundary layers. The original Mt. Iron equations may be used for time averaged concentrations for releases from SLC4 or SLC6, but caution should be used when applying them to long ranges (i.e. off base locations) **where measurements were not made.** Regressions of these types should not be used for atmospheric conditions or locations not included in the measurement domain. Normally, data from the met tower closest to the release site should be used, but we have shown that this may not always give the best predictions, due to passage of the plume from cloud covered to clear skies.

6. Basic Equations

Our next task is to reduce the number of free parameters by using the non-dimensional quantities generally accepted in the modern literature. We must first introduce a few fundamental equations.

In our case, a simple Gaussian plume model predicts a centerline ground-level concentration normalized by release rate as

$$\frac{C_m}{Q} = \frac{1}{\pi U \sigma_y \sigma_z} \quad , \quad (9)$$

where σ_y and σ_z are the lateral and vertical plume parameters for a given downwind distance. An idealized Gaussian crosswind shape also predicts that the surface level cross-wind integrated concentration (CWIC) at a given downwind distance can be calculated from

$$\int C \, dy = \sqrt{2\pi} \, \sigma_y C_m \quad . \quad (10)$$

If the plume is allowed to thoroughly mix through the depth of the well-mixed boundary layer, h , a simple mass balance within the plume requires that

$$C_y = \frac{Uh \int C \, dy}{Q} \equiv 1 \quad , \quad (11)$$

where C_y is the normalized CWIC. Under these same well mixed conditions, mass balancing the Gaussian plume model requires that

$$\frac{C_m}{Q} = \frac{1}{\sqrt{2\pi} U \sigma_y h} , \quad (12)$$

which, in turn, forces the well-mixed vertical plume parameter to be

$$\sigma_z = \sqrt{\frac{2}{\pi}} h . \quad (13)$$

While there is ample evidence for Gaussian profiles of cross-wind concentration from continuous surface sources, vertical mass distributions are often quite non-Gaussian. We apply this equation only as a qualitative check on the well-mixed nature of the plume.

7. The Convective Scaling Approach

The convective scaling approach has been shown to adequately predict diffusion from surface or elevated sources within buoyancy driven boundary layers in numerical models (Lamb, 1982), tank tests (Willis and Deardorff, 1981), and field experiments (Hanna, 1986). Most applications have been to homogeneous terrain, but Sakiyama and Davis (1987) showed success in terrain of varying roughness.

All applications scale results against the dimensionless convective

scaling distance,

$$X = \frac{x w_*}{U h} , \quad (14)$$

where w_* , the convective scaling velocity, is defined as

$$w_* = \left(\frac{g H h}{c_p \rho T} \right)^{1/3} , \quad (15)$$

and where H is surface heat flux, g is gravitational acceleration, and T , c_p , ρ are average temperature within the boundary layer, and specific heat and density near the surface. Note that X can be interpreted as the ratio of the plume travel time (x/U) to an integral time scale of the boundary layer turbulence (h/w_*). Therefore, convective scaling is most applicable when X is fairly close to unity. As X strays from unity, we must have increasing faith that convective turbulence dominates other turbulence sources at scales which may be more appropriate to the plume travel time (e.g. building wakes at short X , mesoscale wind flow variations at large X).

As a conservative "lower limit" for lateral dispersion, Briggs (1985) suggests the following non-dimensional parameterization;

$$\frac{\sigma_y}{h} = \frac{0.6X}{(1+2X)^{1/2}} , \quad (16)$$

which closely approximates Lamb's numerical model and Deardorff's tank tests. Similar equations are presented in the literature for σ_z . Other equations predict the normalized CWIC, C_y . Both quantities approach limits when the plume becomes well mixed through the depth of the boundary layer (roughly $X > 1$).

The basic characteristics of eq. 16 adhere to the theoretical limits of lateral plume growth as predicted by statistics; $\sigma_y \sim x$ for short distances and $\sigma \sim x^{1/2}$ at long range. For example, Draxler's (1976) classical statistical analysis determines dispersion parameters from

$$\frac{\sigma_y}{\sigma_{0X}} = f\left(\frac{t}{T_L}\right) = \left(1 + 0.9\left(\frac{t}{T_i}\right)^{1/2}\right)^{-1} , \quad (17)$$

where t is plume travel time, T_i is an integral time scale proportional to T_L , the Lagrangian time scale. Again, the plume grows linearly for short travel time and as $t^{1/2}$ far from the source.

Field experiments such as Prairie Grass have shown that eq. 16 should be considered as a lower limit to lateral diffusion because low frequency turbulence tends to increase plume spread. Indeed, using hundreds of hours of data, Hanna (1986) showed that the following simple linear equation approximates diffusion of elevated plumes to distances of 50 km;

$$\frac{\sigma_y}{h} = 0.6X \quad . \quad (18)$$

A surface plume release would tend to disperse in a different fashion for short X , but would also follow a linear relationship at distances significantly greater than unity. We must emphasize that this equation holds **on average**, and other more 'controlled' field experiments show growth less than linear for large X . We therefore consider Hanna's equation to be an upper limit for lateral diffusion.

For $X < 4$, the effects of 'top down - bottom up' diffusion have been observed numerically in tank tests and in the field. Materials released near the surface tend to rise or 'loft', while the height of maximum concentration of materials released near the top of the boundary layer tends to lower. Consequently, C_y will be less than unity for $1 < X < 4$, and surface maximum concentration will be less than that predicted with eqs. 9 or 12. The reason is given by the structure of vertical turbulence in convective

boundary layers; downdrafts are strong and spatially confined, while updrafts are weak but distributed over broad regions. As the materials become well mixed in the vertical, the influence of this directional asymmetry wanes.

7. Variation of Convective Scaling Variables

The discussion in the previous section assumes horizontally homogeneous conditions. When we try to select appropriate w_* , U , and h values to calculate the non-dimensional convective scaling distance, X , we quickly discover significant variations in those parameters across the LVDE measurement domain. Commonly, LVDE releases were made under clouds. However, the plume pointed inland and measurements were usually made in clear skies. In Skupniewicz, et al. (1990, 1991b) we measured and modeled changes in boundary layer parameters across the cloud edge. We found that boundary layer mean windspeed were as much as doubled in the vicinity of the edge, and termed this accelerated flow a "cloud breeze". We also found that the boundary layer height increased rapidly within a few kilometers of the edge, but the rise was quickly damped and the total fractional rise was small due to the thick subsidence inversion. In most cases, that rise is within the natural variability of the boundary layer depth, measured at different locations or times. To no surprise, measured surface heat flux was two to four times as large in the sun. Using this heat flux

change, an idealized numerical model adequately simulated the wind speed and boundary layer height modifications at the cloud edge.

Skupniewicz et al. (1991a) describes all meteorological data available from LVDE. Three SODARs were located along the plume trajectory; a permanent facility 1 km downwind of the release site (heretofore identified as "900"), a temporary unit in central Lompoc ("WTP"), and a mobile unit ("trailer"). During most of the HSSF releases (the first 5 of 8 measurement days), the mobile SODAR was positioned along the trajectory between 900 and WTP. During Lompoc Valley releases (the last 3 days), the trailer was at the release site, and there was no intermediate SODAR. A set of solar radiometers was located at the WTP site and near the 900 facility from which surface heat flux was estimated (see Appendix A). Figure 19 shows the fixed SODAR locations with average plume trajectories for each release location.

We cannot produce a detailed picture of horizontal variations in w_* , U or h along the plume trajectory from the available measurements, but we can show that the general characteristics described in Skupniewicz et al. (1991b) were present during LVDE. Figure 20 plots w_* at 900 against w_* at WTP for the times of LVDE tracer measurements. 900 was mainly cloud covered while WTP was almost always sunny. The exceptions are 16 Aug, when clouds were present at Lompoc during some of the tracer measurements, and 17 Aug, when conditions were sunny at all locations. For other

times, we see a twofold increase in heat flux in the sun which produces a 30% increase in w^* . This change in heat flux is somewhat lower than that observed by Skupniewicz et al. (1991b), and we attribute this to a slightly lower boundary layer and less dense stratus.

During 10-12 Aug, all three SODARs were operating, and the mobile one was located in clear skies a few kilometers east of the cloud edge. Figure 21 shows boundary layer height, h , measured concurrently at the three SODARs during LVDE measurements plotted against their average. It is apparent that h rises significantly as the plume exits the clouds, but lowers to roughly its original height at Lompoc. The lowering is contrary to the numerical modeling of Skupniewicz et al. (1991b) based solely on heating changes between cloudy and clear skies, but consistent with some of the measurements at distances well inland from the cloud edge. SODAR measurements at the other permanent Vandenberg facilities, located at the coast to the north and south of 900 (mostly cloud covered), generally agree with the 900 and WTP values. While high, the trailer values are within the range of variability. Unfortunately, we do not have other boundary layer heights at more inland sites to better define h in the clear skies. We conclude that while the h increase at the cloud edge is significant, the available measurements indicate that h relaxes to its original height at Lompoc, the eastern edge of the LVDE domain.

LVDE Tracer Trajectories

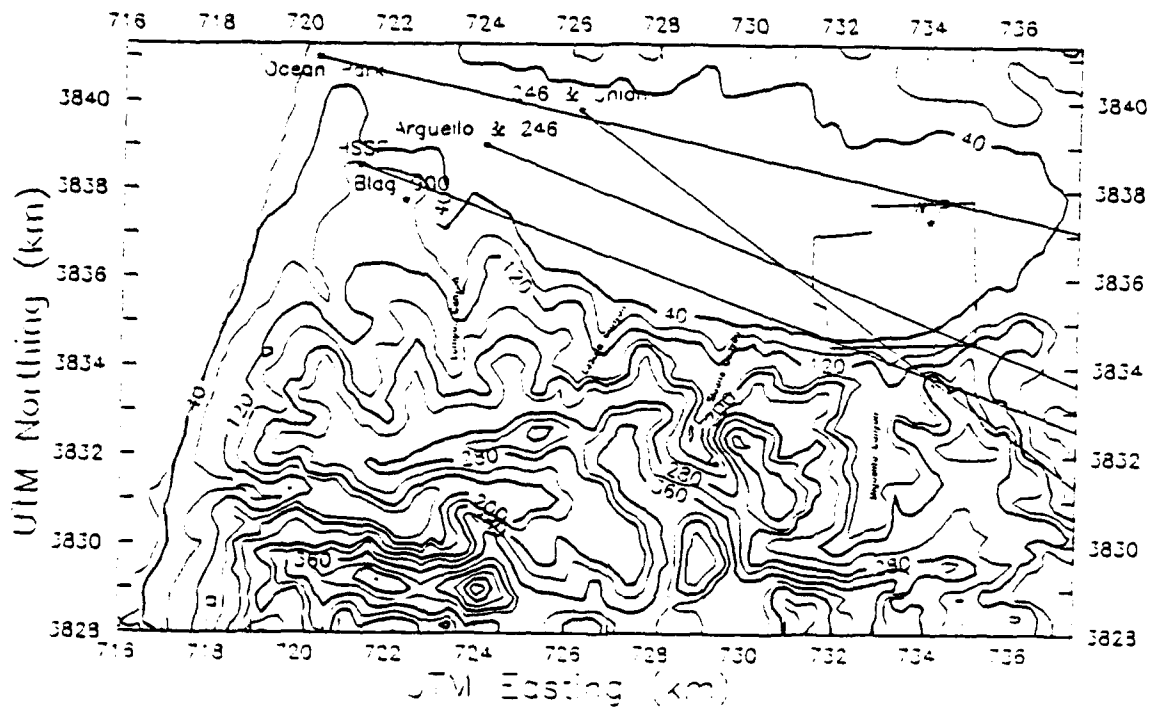


Figure 19. Topographic map of the LVDE domain. Lines are average plume trajectories for each release site. Permanent SODARs were located at Bldg. 900 and WTP. A third temporary SODAR was located at various intermediate positions along the plume trajectory.

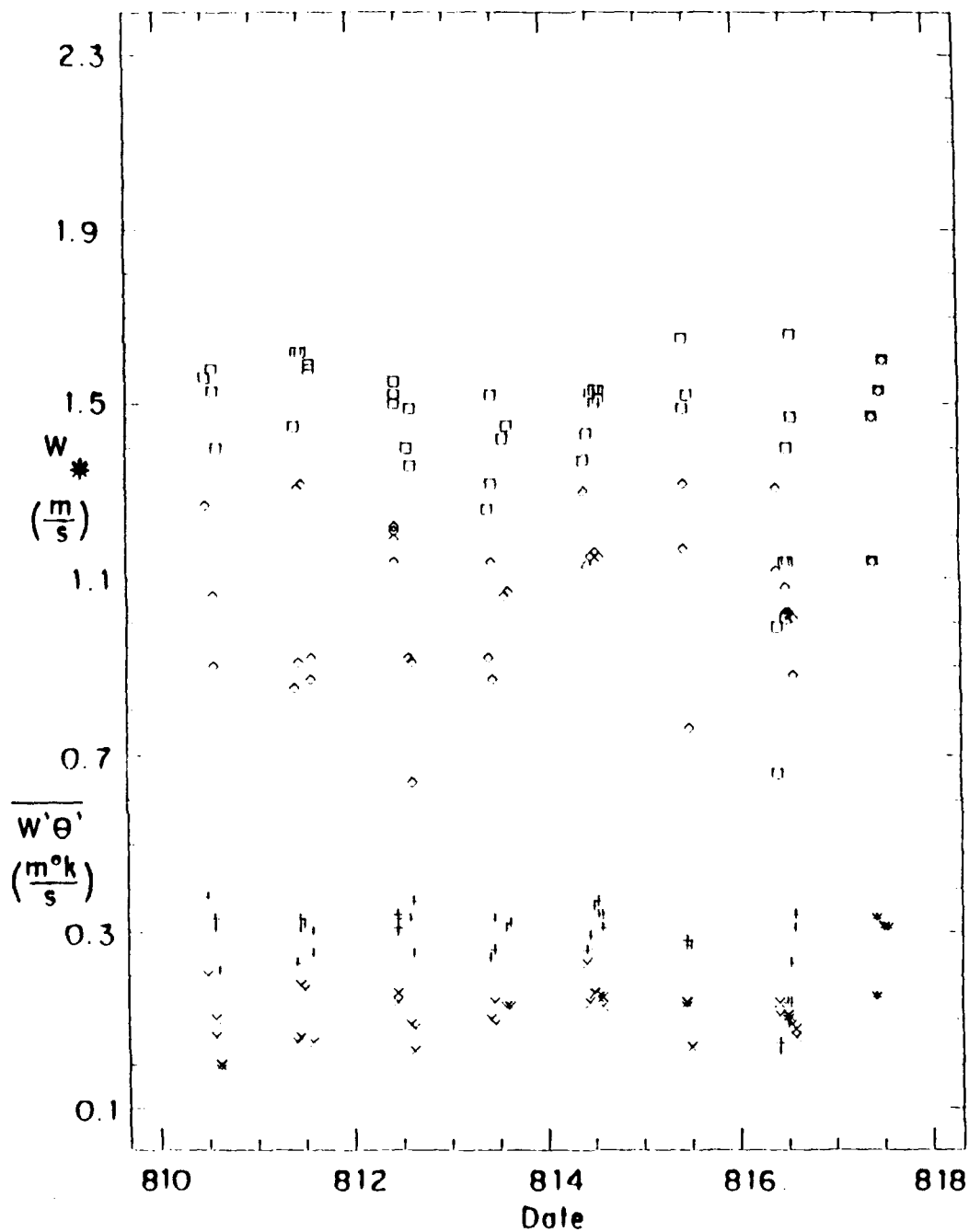


Figure 20. Surface heat flux at the Water Treatment Plant (+) and the release site (X). w_* at the Water Treatment Plant (squares) and the release site (diamonds). Data are one hour averages centered on the time of release for each LVDE cross wind plume transect.

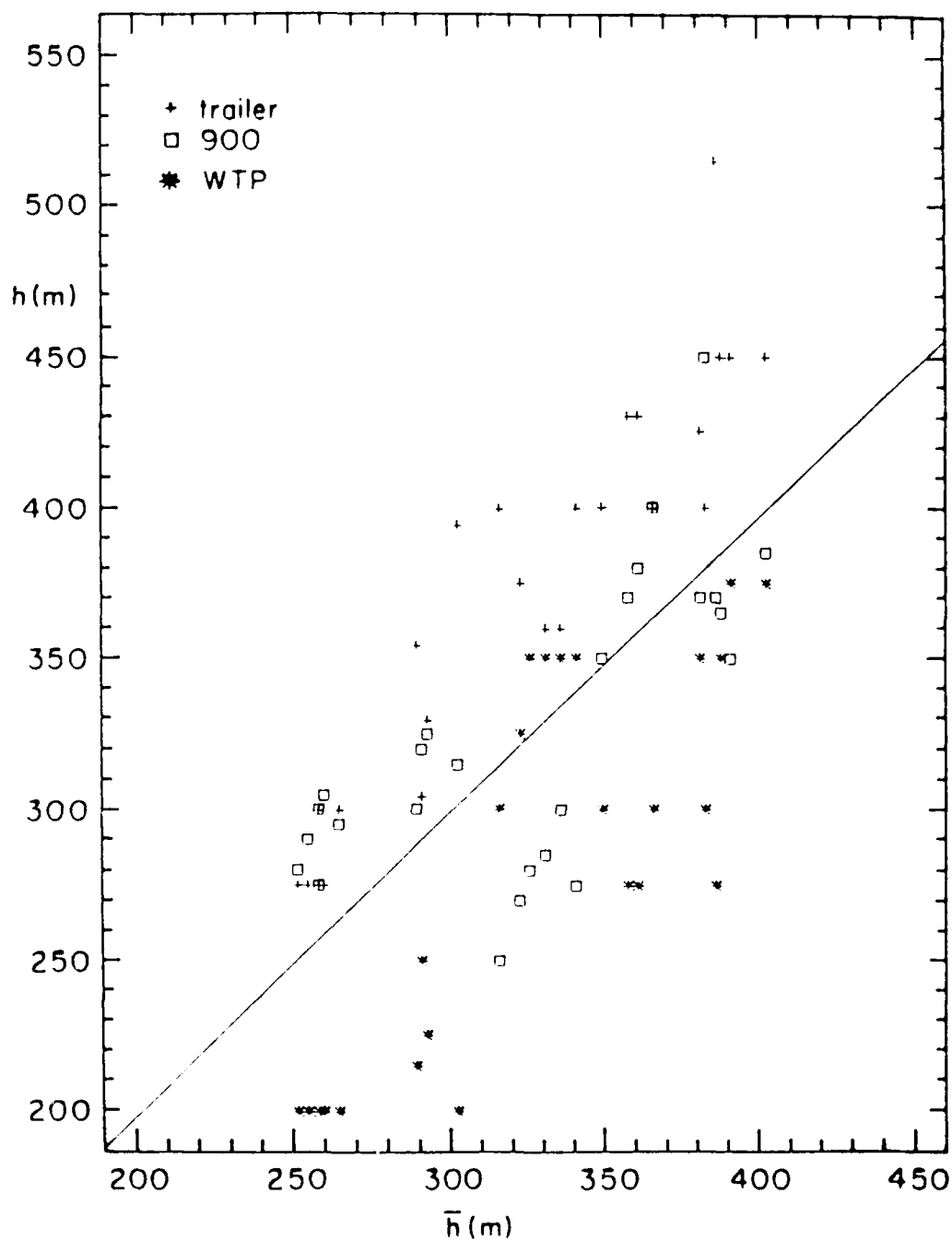


Figure 21. Boundary layer heights near the release site (Building 900), a midpoint along the plume trajectory (trailer), and in the city of Lompoc (WTP) for times corresponding to plume transects. Data at the three locations are plotted against their average.

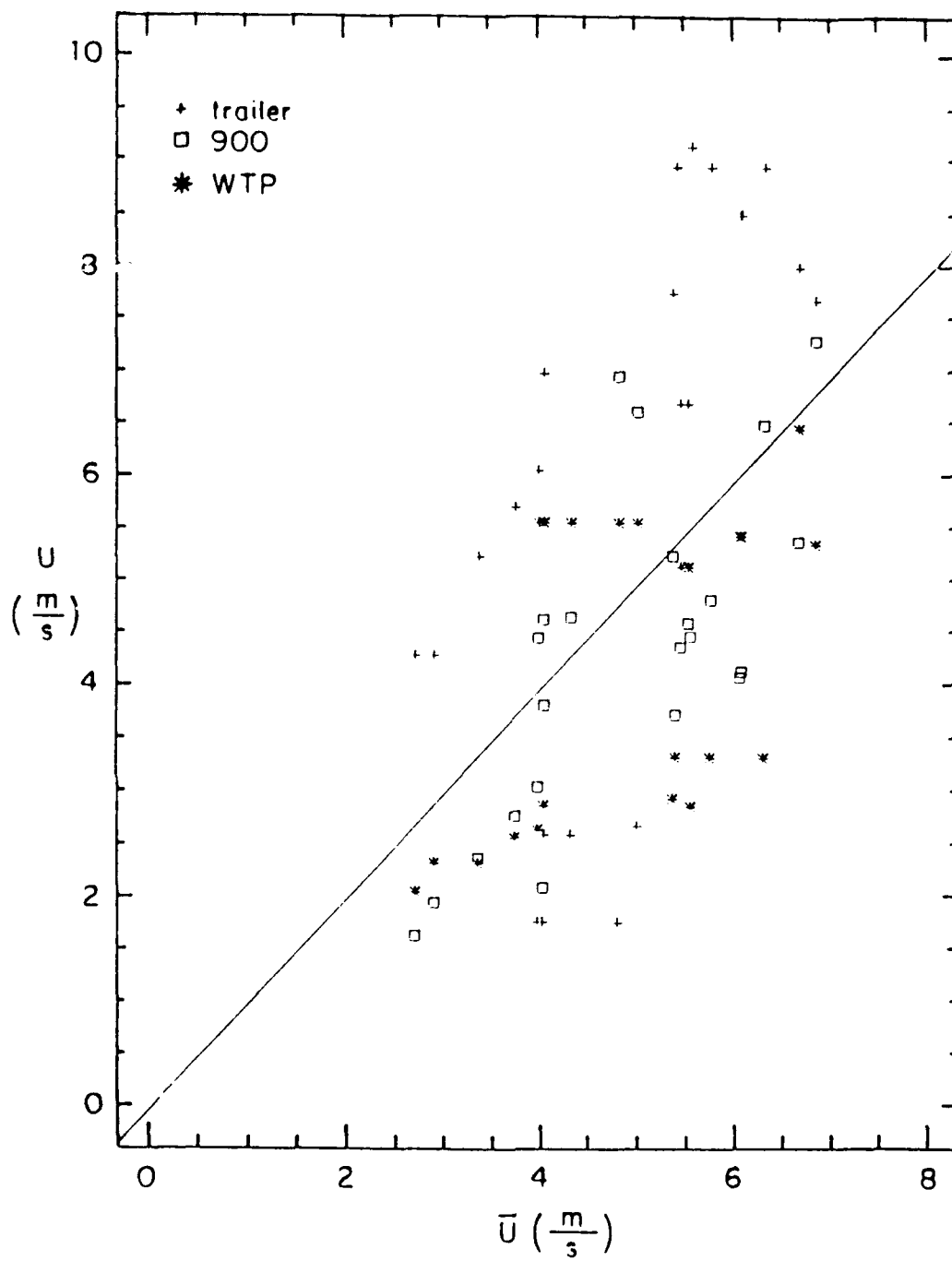


Figure 22. Boundary layer vector average wind speed near the release site (Building 900), a midpoint along the plume trajectory (trailer), and in the city of Lompoc (WTP) for times corresponding to plume transects. Data at the three locations are plotted against their average.

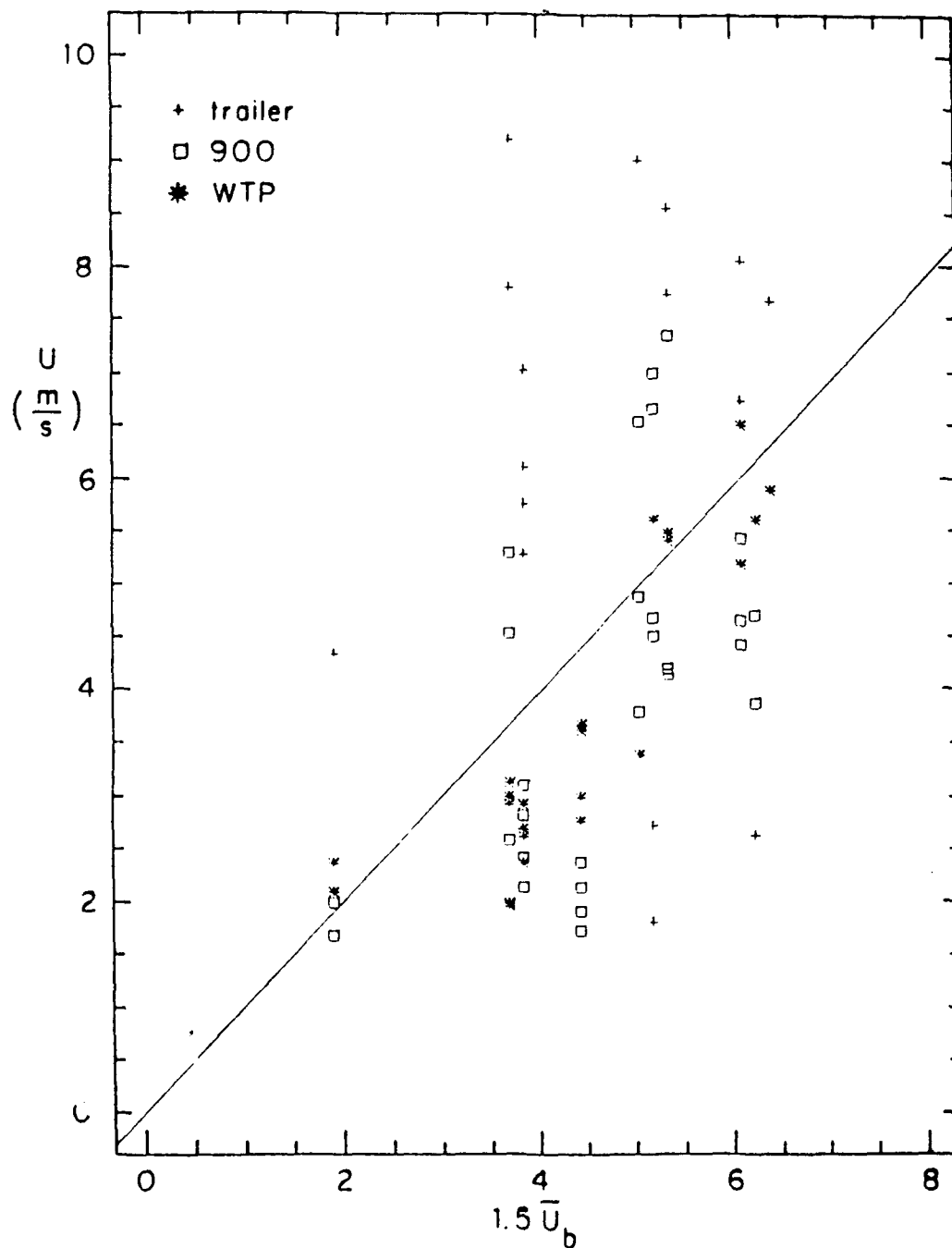


Figure 23. Boundary layer vector average wind speed near the release site (Building 900), a midpoint along the plume trajectory (trailer), and in the city of Lompoc (WTP) for times corresponding to plume transects. Data at the three locations are plotted against the vector average of 12 ft wind speeds measured at 24 towers within 20 km of the release site multiplied by the factor 1.5.

In a similar fashion, wind speeds averaged through the depth of the boundary layer are plotted against their average in fig. 22. In most cases, speeds at the trailer are significantly higher than speeds at 900 and WTP, which generally agree with each other. Again, this pattern agrees with the conceptual model of the "cloud breeze" proposed by Skupniewicz et al. (1991b). As with the boundary layer heights, our data show that the speed enhancement was negligible at the eastern edge of the measurement field.

Wind estimates from one or more SODARs were often unavailable due to the degrading effects of stratus or equipment failure. Therefore, we would like to use tower measurements to estimate boundary layer average wind speed. Figure 23 plots the average of all operating 12 ft wind speeds (maximum 24 towers) against the three SODAR measurements discussed above. After adjusting the 12 ft speeds by the factor 1.5, the characteristics of fig. 22 are duplicated with similar scatter. Such an ad hoc wind speed estimate is advised only when true field measurements are available for calibration.

8. Convective Scaling Applied to LVDE

Clearly, the parameters that determine the non-dimensional convective scaling distance, X , are changing along the trajectory

of the plume. To demonstrate the general characteristics of plume parameters, we assume horizontally homogeneous conditions for each plume measurement. Later, we allow a change in scaling based on the position of the cloud edge along the plume trajectory.

We consider only hourly averaged plume parameters for this analysis. For each data point, time averages of meteorological quantities are centered upon the estimated time of release, after adjustment by the approximate plume travel time. In the following, we calculate X with the average w^* measured at SODARs 900 and WTP (fig. 20), h estimated from the average of the three SODARs (fig. 21), U estimated from the adjusted base average wind speed (fig. 23).

Figure 24 shows growth in the lateral plume dimension, σ_y . Also shown are the Briggs (1985) and Hanna (1986) formulations we consider to be the lower and upper limits. We see that most data lie between the two limits. The few data points below $X = 1$ agree with the lower limit. The plume grows rapidly near $X = 1$, then slowly to a distance of roughly $X = 5$. The plume again expands rapidly beyond $X = 6$.

For each transect σ_y was calculated directly with the "moment method" and indirectly by applying eq. 10 ("maximum method"). Averaging was performed with eqs. 7-8. The pattern described above is repeated for both methods. Since very little difference is

observed, we use the more direct moment method σ_y from this point forward. Data obtained during the Lompoc Valley release are depicted as shaded symbols. We found differences between the release locations negligible, so we keep all data grouped together.

Figure 25 shows the normalized CWIC, C_y , calculated directly with eq. 11, and indirectly by applying eq. 10 to eq. 11. Data below $X = 6$ tend to cluster about unity, implying that the plume is well mixed in the vertical. Plume lofting would be indicated by a decrease in C_y from $X = 1$ to $X = 4$, and we see no evidence of this effect. Unexpectedly, C_y data beyond $X = 6$ are significantly larger than unity. This implies an increase in plume mass measured at the surface, contrary to intuition. We will offer a plausible explanation for this anomaly later.

We identify Lompoc Valley releases in fig. 25 with shaded symbols, and we see no reason to separate C_y data into subsets based on their respective release locations.

To further test the assumption of a vertically well mixed plume, we estimate σ_z , the vertical plume dimension, with eq. 9 and take the ratio of σ_z and the theoretical limit calculated from eq. 13. Figure 25 shows values near or above unity with no upward trend, indicating that the plume has arrived at its limiting vertical dimension, if no plume lofting has occurred. Again we see a change at roughly $X = 6$, where the plume appears to be shorter

than its limiting value. This trend is undoubtedly an artifact of the increased CWIC measured at the surface and noted above.

Figure 26 shows maximum concentrations normalized by release rate calculated with three different methods. In contrast to the σ_y methods, the "maximum method" is the more direct measurement while the "moment method" implies maximum concentration from eq. 10. A third method shown in fig. 26 uses eq. 12, assuming the plume is well mixed in the vertical. The maximum and moment method closely agree, while the "well mixed method" agrees with the others only for distances less than $X = 6$. Beyond that point the "well mixed method" is lower than the others, presumably due to the rapid lateral expansion of the plume. We use the direct measure of maximum concentration from this point forth.

The Lompoc Valley releases, indicated in fig. 26 with shaded symbols, are somewhat lower and tend to segregate from the HSSF releases. We recall observing lower Lompoc Valley centerline concentrations in the regression analysis. Due to the large scatter, data sparsity, and lack of similar differences in σ_y or C_y , we consider the lower Lompoc Valley C_0/Q values a statistical anomaly and thus will keep all measurements grouped together.

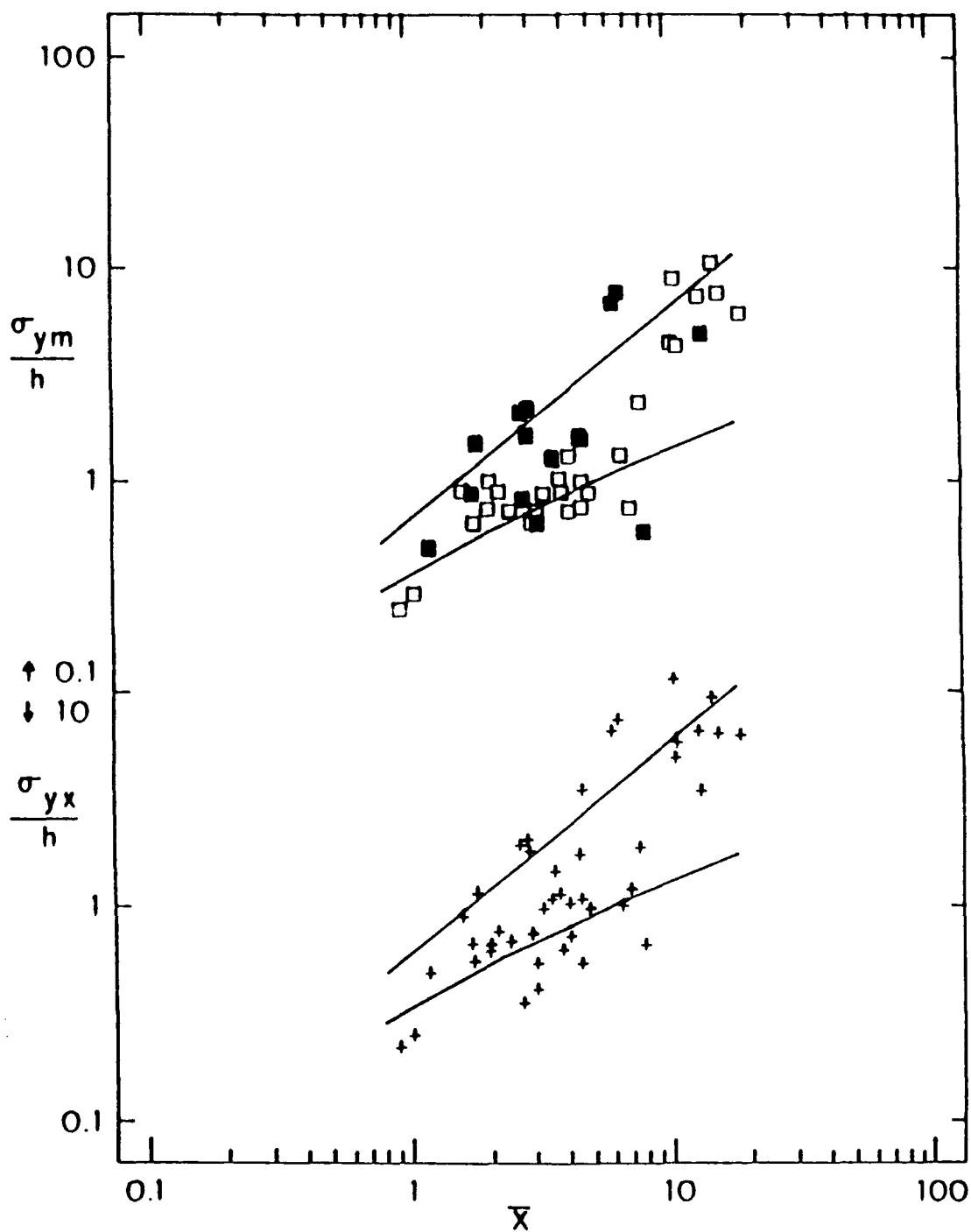


Figure 24. One hour averaged lateral plume spread as a function of average nondimensional distance. σ_{ym} is estimated from moment calculations of the cross wind mass distribution and σ_{yx} is estimated from eq. 10. For each case, upper line is the upper limit as defined by eq. 18 and the lower line is the lower limit, eq. 16. For σ_{ym} , shaded symbols indicate Lompoc Valley releases.

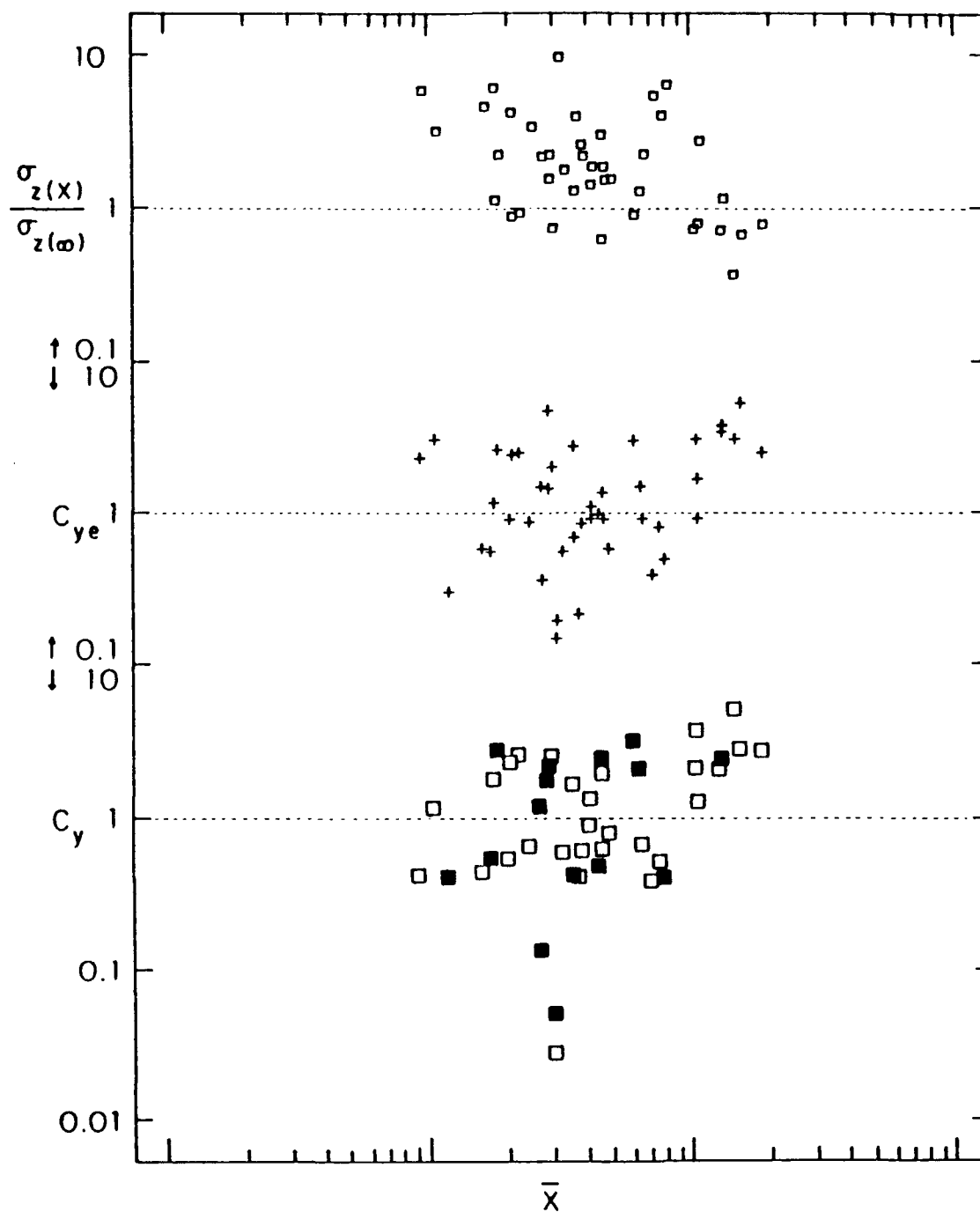


Figure 25. Normalized cross wind integrated concentration, C_y , calculated directly (eq. 11), and estimated by substitution of eq. 10 into eq. 11 (C_{ye}) as a function of average nondimensional distance. For C_y , shaded symbols indicate Lompoc Valley releases. Also, ratio of eq. 9 estimate of vertical plume spread, σ_z , to its well-mixed limit (eq. 13).

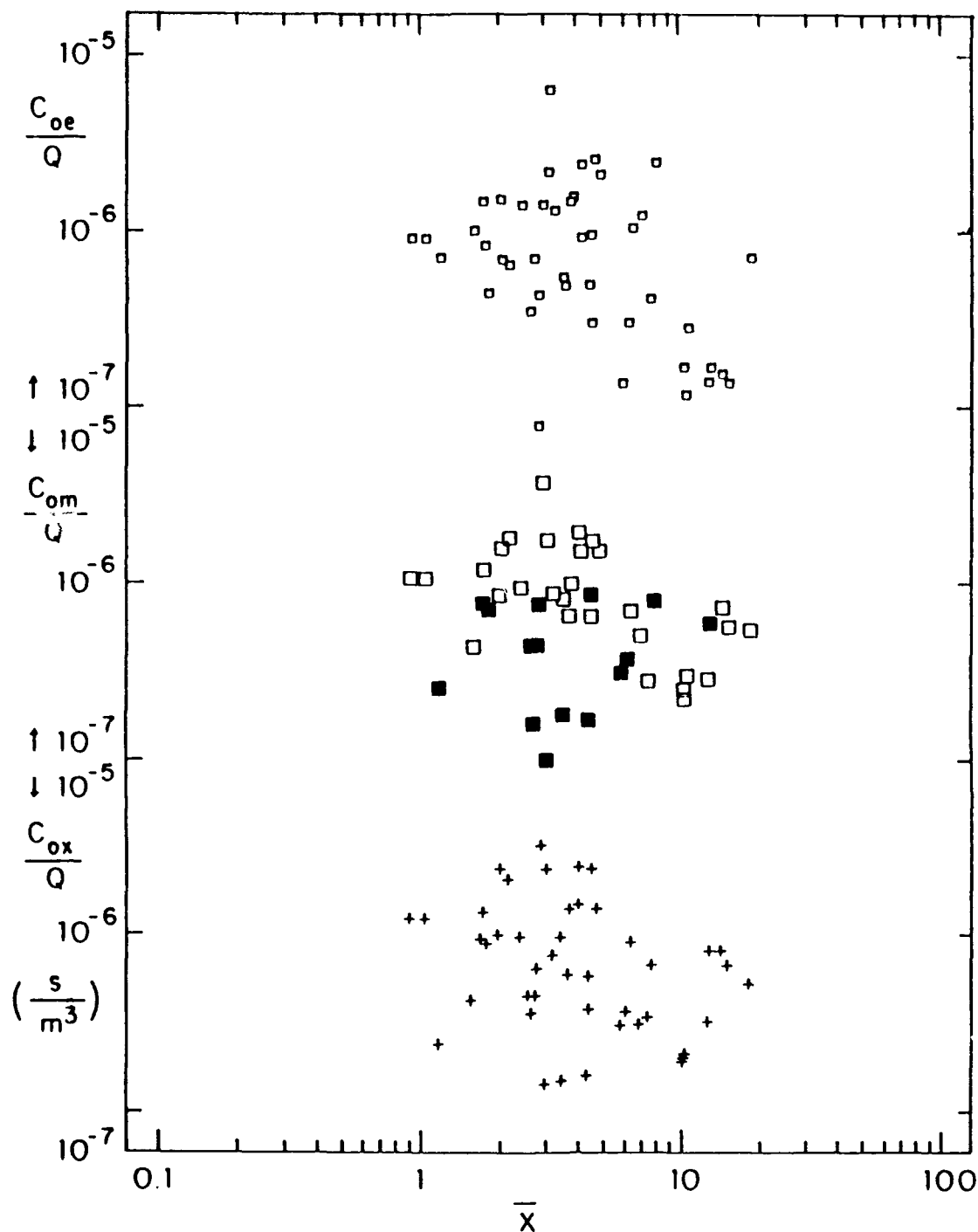


Figure 26. Normalized surface maximum concentration measured directly, C_{ox}/Q , and approximated from eq. 10 (C_{om}/Q) as a function of average nondimensional distance. For C_{om}/Q , shaded symbols indicate Lompoc Valley releases. Also, C_{oe}/Q is estimated assuming plume is well-mixed through the boundary layer (eq. 12).

9. Two Zone Convective Scaling

The approach we take is to consider the domain as two zones demarcated by the cloud edge. For each measurement, we have calculated the approximate location of the cloud edge along the plume trajectory based on hourly GOES satellite images. Appendix B details our methodology for this procedure. We have already described changes in w_* , U , and h attributed to the cloud edge. Here, we only consider a step change in w_* at the edge, maintaining the average values of U and h used previously. We would prefer to allow all scaling parameters to vary, but we cannot detail the changes in U or h along the plume trajectory based on our measurements. Such a model input requirement would certainly be difficult from an operational standpoint.

Refer to fig. 27. Let curves 1 and 2 define plume growth referenced to non-dimensional distance calculated from scaling parameters under the stratus (zone 1) and in the sun (zone 2), respectively. Curve 3 defines a plume which crosses the zone 1-2 boundary. In our case, this boundary is the cloud edge, X_C . We assume that the plume grows with zone 2 scaling, as if it had been released from a virtual source, X_V , some distance between $X=0$ and X_C .

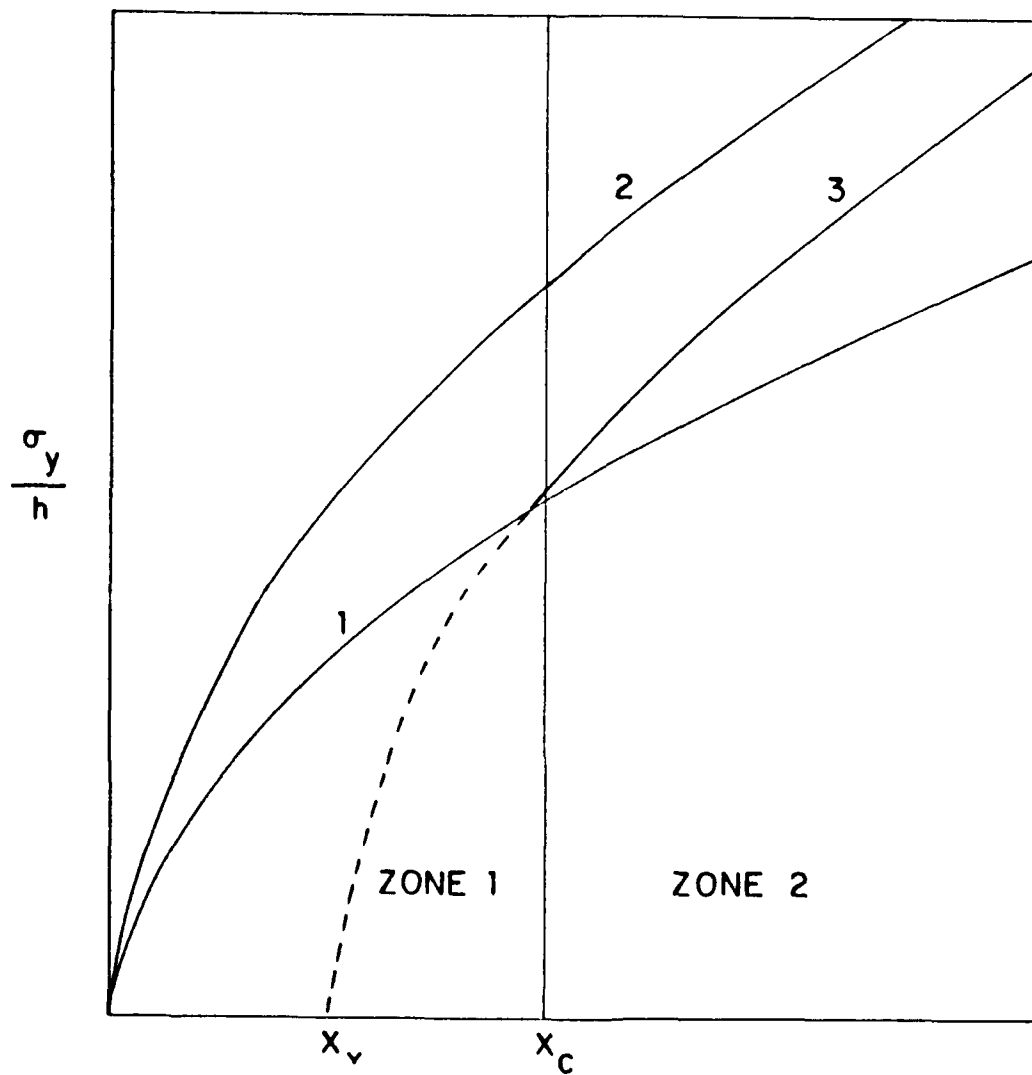


Figure 27. Schematic of two zone convective scaling for lateral plume spread. For LVDE, zone 1 is cloud covered and zone 2 is cloud free. Curve 1 defines plume growth in zone 1 coordinates, curve 2 defines growth in zone 2 coordinates. Two zone parameterization follows curve 1 in zone 1 and curve 3 in zone 2. x_c is the cloud edge and x_v is the virtual source (e.g. eq. 23).

The function defining curve 3 can take many forms, depending on the choices for curves 1 and 2. One choice is the Briggs formulation (eq. 16). Calculating X with scaling parameters valid in zone 1, curve 2 is defined by

$$\frac{\sigma_{y2}}{h} = \frac{0.6FX}{(1+2FX)^{1/2}} \quad , \quad (19)$$

where F is the ratio of the respective scaling parameters,

$$F = \frac{\frac{w_{*2}}{U_2 h_2}}{\frac{w_{*1}}{U_1 h_1}} \quad , \quad (20)$$

In our case, we assume U and h are constant (averaged over the domain), so $F = w_{*2}/w_{*1}$. Curve 3 is defined by the set of equations

$$\frac{\sigma_{y3}}{h} = \frac{0.6X}{(1+2X)^{1/2}} \quad X \leq X_c \quad (21)$$

$$\frac{\sigma_{y3}}{h} = \frac{0.6F(X-X_c)}{(1+2F(X-X_c))^{1/2}} \quad X > X_c \quad (22)$$

$$X_v = \frac{(F-1)}{F} X_c , \quad (23)$$

The equation for X_v is obtained by matching the two previous equations at X_c . One can see that F can take any value, so we can equivalently choose to model a plume entering a stratus covered domain from the clear skies.

We have stated earlier that eq. 16 should be considered a lower limit. We suggest a generic parameterization which fits most lateral plume growth formulations suggested in the literature:

$$\frac{\sigma_y}{h} = AX^a \quad X < X_{01} \quad (24)$$

$$\frac{\sigma_y}{h} = AX_{01}^{(a-b)} X^b \quad X_{01} < X \leq X_c \quad (25)$$

$$\frac{\sigma_y}{h} = AX_{01}^{(a-b)} (F(X-X_v))^b \quad X > X_c \quad (26)$$

$$X_v = X_c - \frac{X_c}{F} \left(\frac{X_{01}}{X_{02}} \right)^{\left(\frac{a-b}{b} \right)}, \quad (27)$$

where A, a, b, X_{01} , and X_{02} are free parameters and $X_c > X_{01}$. Most short range experiments and numerical modeling results would require $A = 0.6$ and $a = 1$ (i.e., Prairie Grass). Since we have few data for $X < 1$, we use these values. b determines growth at large distances, and is in the range of 0.5 to 1. We prefer to use $b = 2/3$ as suggested by Deardorff and Willis (1975), Lamb (1979), and Briggs (1985).

X_{01} and X_{02} are the distances at which plume growth transitions from x^a to x^b in zones 1 and 2, respectively. Conceptually, the transition occurs when the width of the plume has exceeded the dominant scale of the convective energy producing eddies. Selecting a transition point value of 0.18 adequately reproduces the numerical modeling results of Lamb (1979) and the tank tests of Deardorff and Willis (1975). Briggs (1985) suggests that a transition at $X = 0.6$ provides a better match to field experiments.

We contend that the transition points of zone 1 and zone 2 can be different. Pasquill and Smith (1983) shows that we can calculate plume spread by integrating the Lagrangian turbulence spectrum after applying a low pass filter at a frequency inversely

proportional to the plume travel time. Therefore, the transition point should occur when the travel time is near the Lagrangian time scale. Thinking in terms of spectral similarity in the convective boundary layer (e.g. Hojstrup, 1982), the peak in the Eulerian lateral energy spectrum occurs near

$$n_m = \frac{f_m h}{U} = \frac{h}{T_m U} = 0.5 \quad , \quad (28)$$

where f_m is the frequency corresponding to a dominant eddy time scale T_m . By definition,

$$X_1 = \frac{w_{*1} X}{hU} = \frac{w_{*1} t_1}{h} \quad , \quad (29)$$

where t_1 is plume travel time to X_1 . So, it follows that

$$X_1 \propto \frac{w_{*1} T_m}{h} \propto \frac{w_{*1}}{U} \quad . \quad (30)$$

Since we use an average wind speed and w_{*1} is smaller than w_{*2} we contend X_1 should be smaller than X_2 . The proportionality constant in eq. 30 depends on the Eulerian-Lagrangian time scale ratio which is difficult to measure or estimate, so without detailed spectral

information we state only that the constant may also be different in zones 1 and 2. Fortunately, the model is not extremely sensitive to these parameters. Using reasonable values obtained from the literature, we choose $X_1 = 0.18$ (approximating Lamb, 1979) and $X_2 = 0.60$ (Briggs, 1985).

With these assumptions, the generalized equations reduce to

$$\frac{\sigma_y}{h} = 0.6X \quad X < 0.18 \quad (31)$$

$$\frac{\sigma_y}{h} = 0.34 X^{2/3} \quad 0.18 < X \leq X_c \quad (32)$$

$$\frac{\sigma_y}{h} = 0.34 (F(X - X_v))^{2/3} \quad X > X_c \quad (33)$$

$$X_v = \frac{(F - 0.55)}{F} X_c \quad , \quad (34)$$

10. Convective Scaling Model Comparison - General

In this section, we compare measurements of σ_y , C_0/Q , and C_y

against the two zone model proposed above and four models outlined earlier. For all cases, C_0/Q and C_y are calculated from eqs. 10-12 after calculation of σ_y . The four test models are 1) Briggs' eq. 16 obtained from scaling parameters in zone 1 and thus considered the "lower limit", 2) Hanna's eq. 18 obtained from scaling parameters in zone 2, considered the "upper limit", 3) Briggs' (1985) "best fit" recommendation (eqs. 24 and 25 with $A = 0.6$, $a = 1$, $b = 2/3$, and $X_1 = 0.6$) obtained from scaling parameters in zone 2, considered an intermediate choice, and 4) Draxler's (1976) statistical approach (eq. 17) applied to LVDE data.

We have only briefly described the statistical approach. This method requires good measurements of turbulence intensity, σ_θ . We use the 10 minute average value measured by Vandenberg's 3-axis Gill anemometer at Building 900, the bivane mounted on Tower 057, or the trailer's sonic anemometer, depending on the release site and data availability. The method is only valid for plume travel times within roughly an order of magnitude of the Lagrangian time scale. This method gives reasonable results only after excluding the above described long range data, where rapid cloud expansion occurs. Figure 28 shows the results after this editing. The derived integral time scale, $t_i = 330$ sec, is within the range of values calculated by Draxler for surface releases.

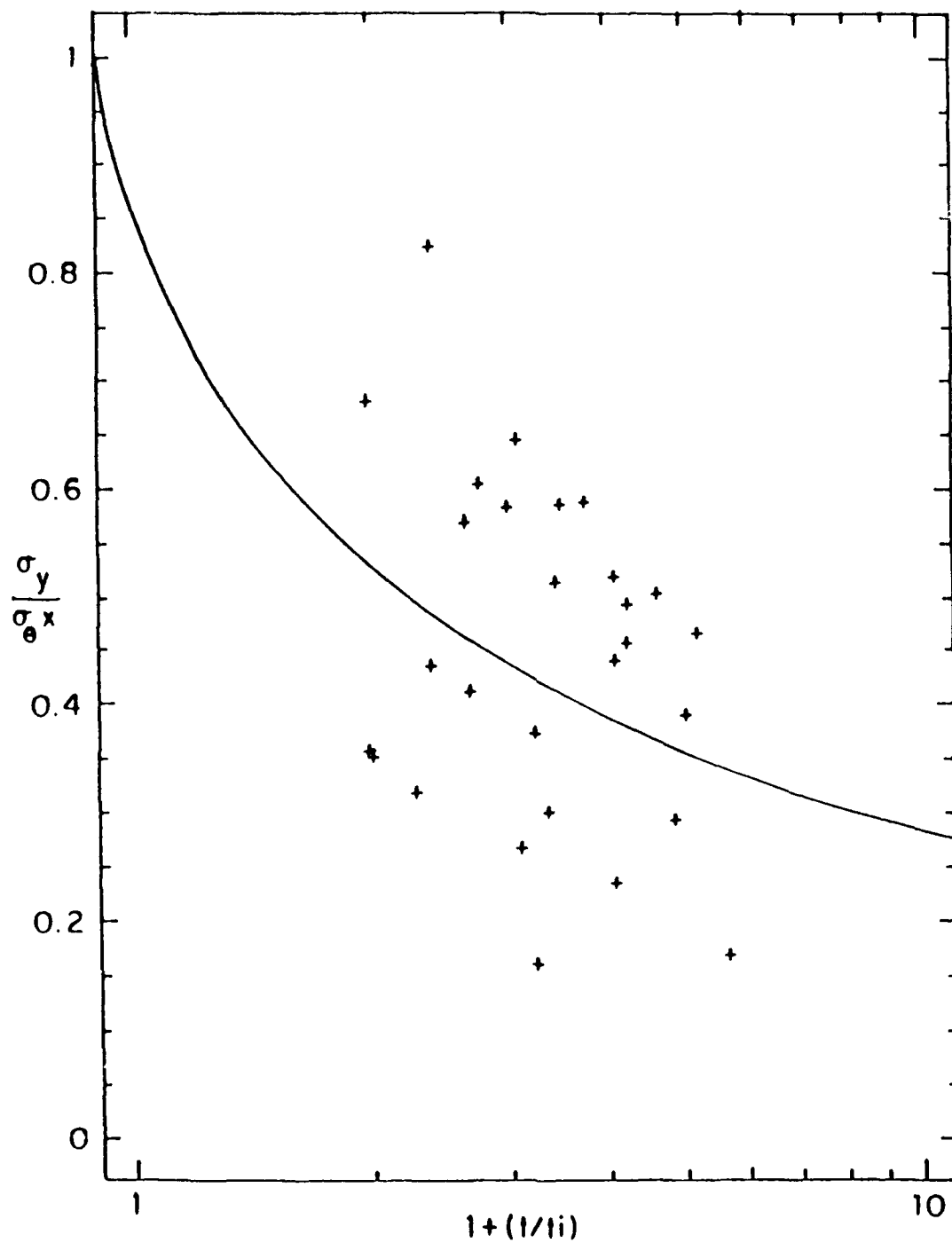


Figure 28. Draxler's (1976) statistical approach applied to LVDE. + are measured values and squares, line are eq. 17 with $t_i = 330$ seconds. Due to rapid cloud growth at long distances from the source, only data with travel times less than 2000 seconds were considered.

Figures 29 and 30 show the comparison for σ_y . Models 1 (lower limit) and 2 (upper limit) underpredict and overpredict plume spread in a similar fashion to fig. 24, where all scaling parameters were averaged. Model 3 (intermediate) slightly overpredicts σ_y at short distances ($X < 6$), and underpredicts for $X > 6$. Models 4 (Draxler) and 5 (two zone) do a good job at short range, then underpredict at long range. The deficit at long range is eliminated for the two zone model only if the σ_y predictions are doubled. We show this arbitrary adjustment in the figures.

We might conclude that either model 4 or 5 may be used for distances less than $X = 6$. We caution use of model 4 for meteorological conditions or locations different from those of LVDE. This semi-empirical model depends critically upon the integral time scale chosen. There is no guarantee that the time scale is valid for other conditions or locations. σ_θ was measured directly in the path of the plume with fast response instruments. Using the slower response tower wind vanes at other locations will reduce σ_θ and the predicted plume dimensions. On the other hand, the two zone model is purely theoretical and does not depend on direct turbulence measurements.

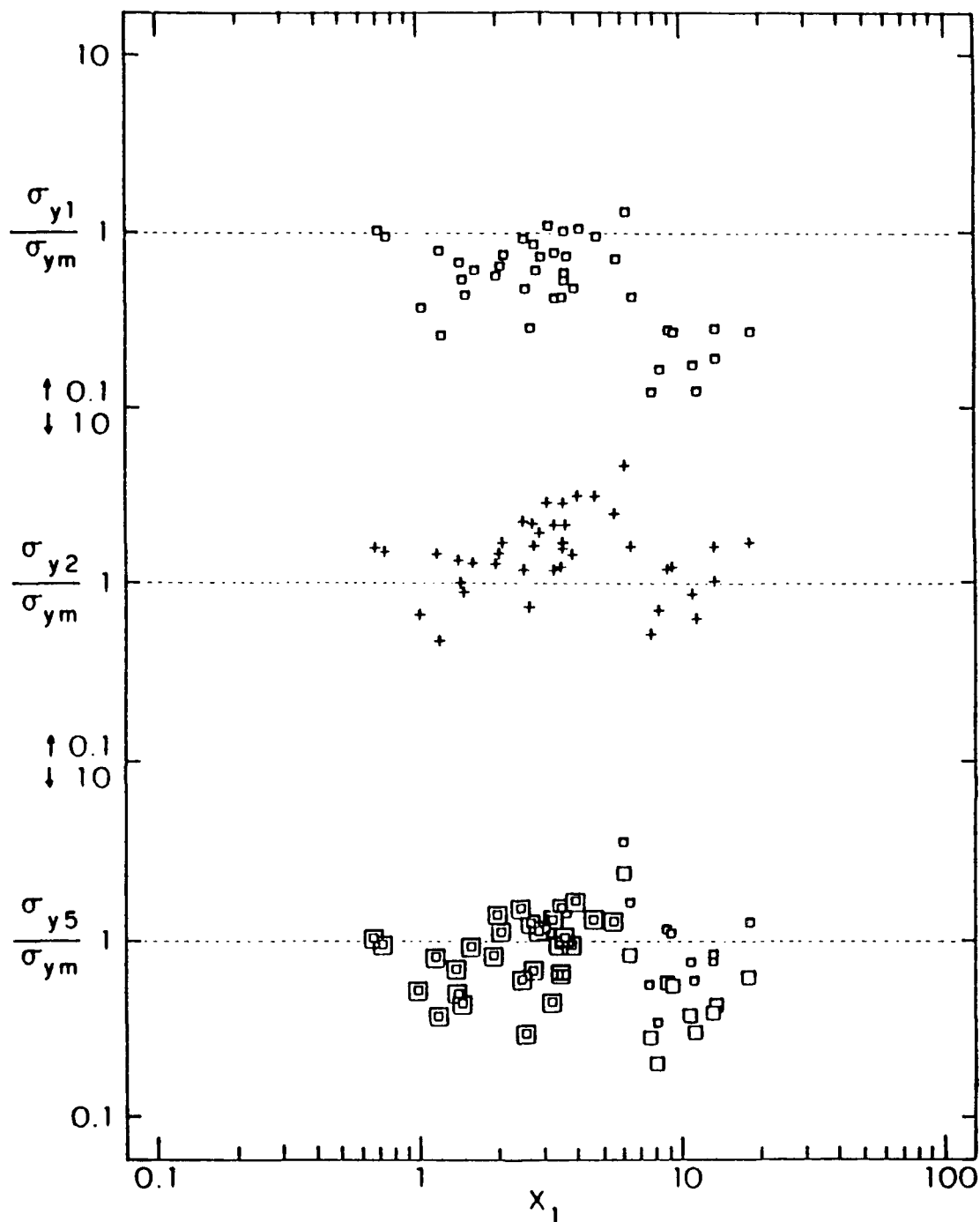


Figure 29. Ratio of predicted to measured lateral plume spread as a function of nondimensional distance calculated from scaling parameter measured at the source (zone 1). Model 1 is assumed lower limit (eq. 16), model 2 is assumed upper limit (eq. 18), and model 5 is two zone (eqs. 31-34). For model 5, small squares at $X > 6$ are model 5 predictions multiplied by a factor two.

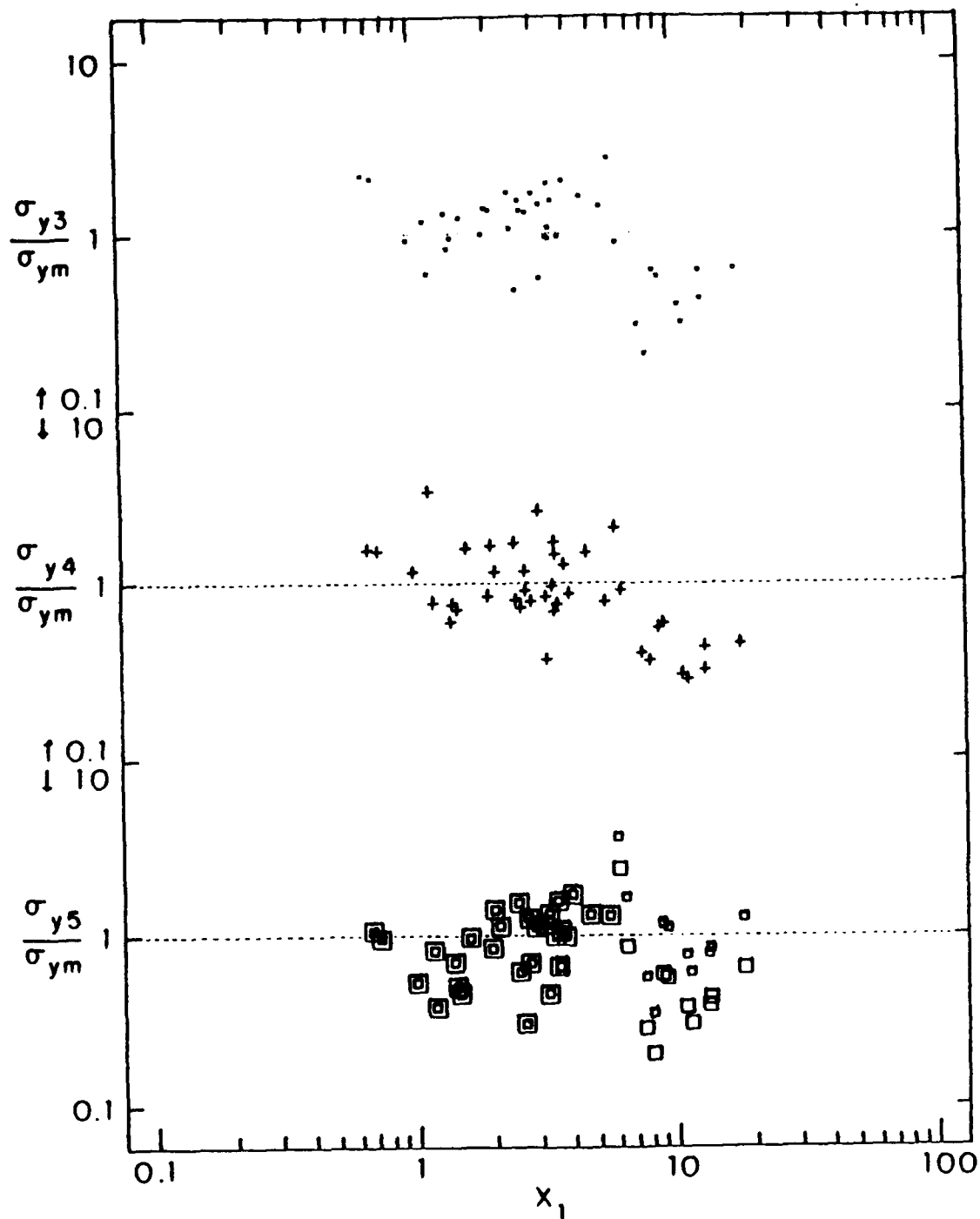


Figure 30. Same as figure 29, except model 3 is Briggs' (1985) recommendation and model 4 is eq. 17 statistical estimate.

Figures 31 and 32 show C_0/Q predictions. The "limit" models (1 and 2) poorly predict maximum concentration. Model 4 (Draxler) slightly overpredicts centerline concentration. Models 3 and 5 do a reasonable job at all ranges, except for a few points at the furthest range. The rapid expansion of the plume at $X > 6$, mentioned earlier, is not reflected in the C_0/Q measurements. If this were true, we would see a sharp decrease in centerline concentration beyond $X = 6$. We offer a plausible explanation later.

Figures 33 and 34 show C_y predictions. An agreement between observation and model indicates conservation of mass at the surface. Again, the lower and upper limit models are severely biased at all ranges. Only Draxler's model (4), the two zone model (5) adequately predicts C_y for $X < 6$. No model gives adequate prediction for all ranges because observations of C_y sharply increase beyond $X = 6$. As the figures show, arbitrarily doubling σ_y for the two zone model at $X > 6$ also reasonably adjusts the C_y prediction.

In summary, the two zone formulation adequately predicts σ_y , C_0/Q , and C_y as judged by a comparison with the four models based on homogeneous conditions. No model properly predicts all quantities for $X > 6$. Only by arbitrary adjustment of predictions at these ranges do we simulate σ_y and C_y data. Oddly, this adjustment is

unnneeded for C_0/Q .

Figure 35 illustrates the following argument. When we closely examined the raw data for points beyond $X = 6$, we saw very "flat" or bimodal instantaneous cross-wind concentration distributions. Referring to fig. 19, all these data were measured at downwind distances beyond LaSalle Canyon. We contend that the shear created by the ventilating effects of Sloan and Miguelito Canyons rapidly expands the lateral dimensions of the plume at the surface. One need only briefly visit Miguelito Canyon to realize that the daytime flow at the surface is distinctly up-canyon. Closer to the coast, near surface up-valley flow is negligible, such as in the cooler Lompoc Canyon. The low level northerly surface winds of the inland side canyons are in sharp contrast to the general west-northwest flow over the region, as indicated by plume trajectories and SODAR winds. Because the up-canyon flow is so shallow, mass removed from the "main" plume is quickly replaced by mass from aloft through vertical mixing. The net result is a wide, flat surface concentration distribution. The cross-wind integrated concentration increases, as if the plume were gaining mass.

The above arguments are speculative, but are consistent with our observations. Only a mesoscale numerical model which accurately captures the main features of these up-canyon flows could unambiguously determine the actual causes.

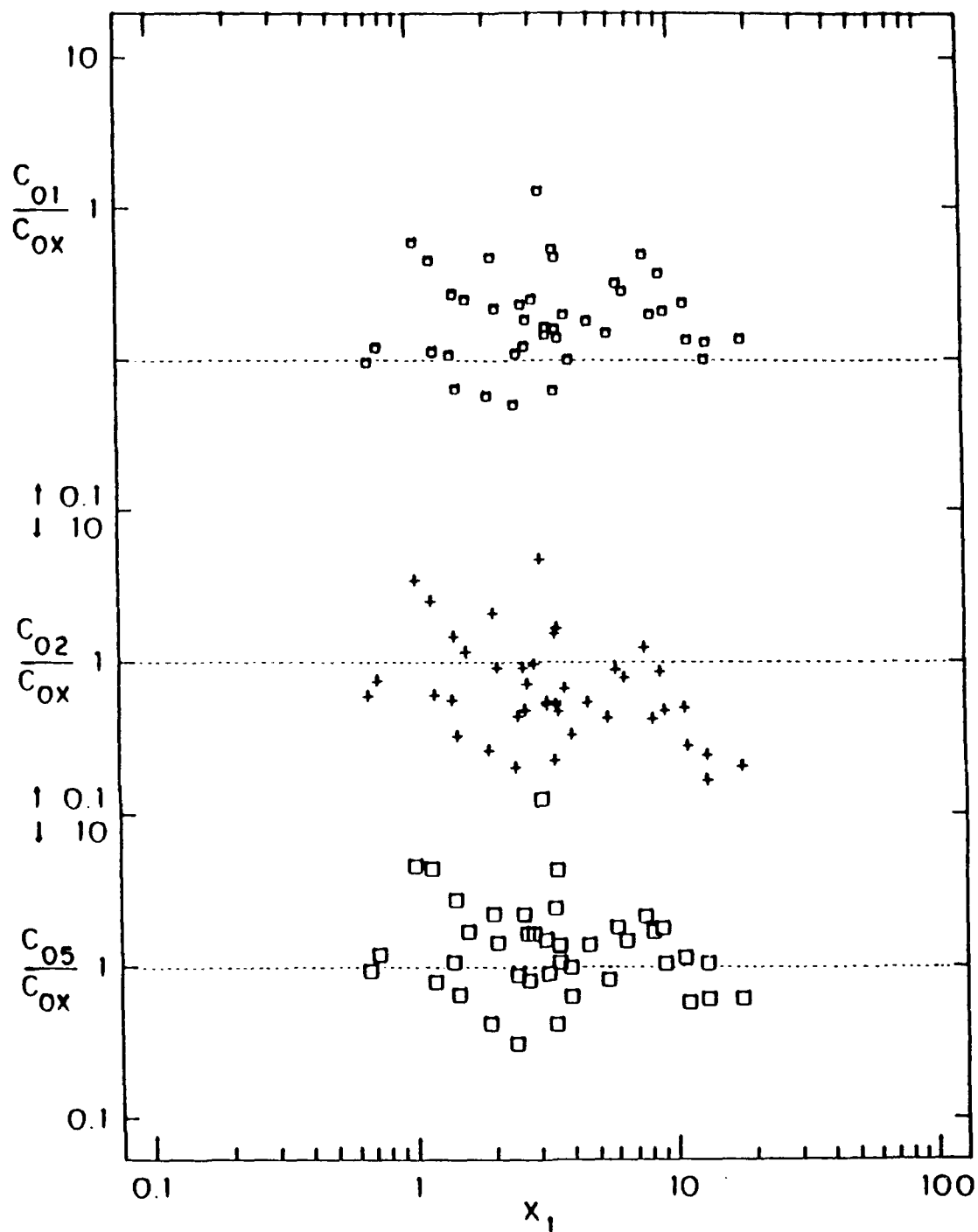


Figure 31. Ratio of predicted to measured surface maximum concentration as a function of nondimensional distance calculated from scaling parameter measured at the source (zone 1). Models are identified in fig. 29.

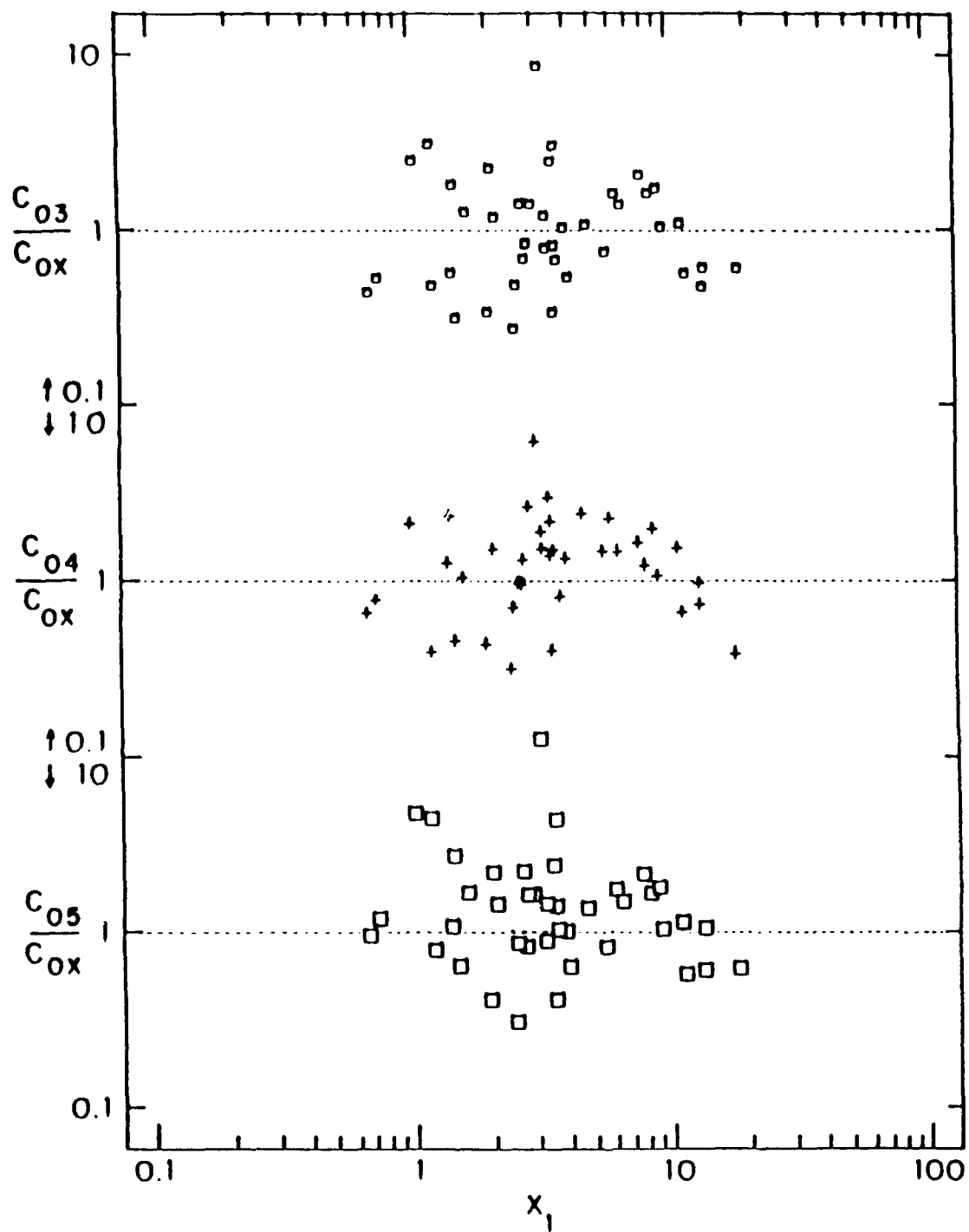


Figure 32. Same as fig. 31, except for models 3, 4, and 5.

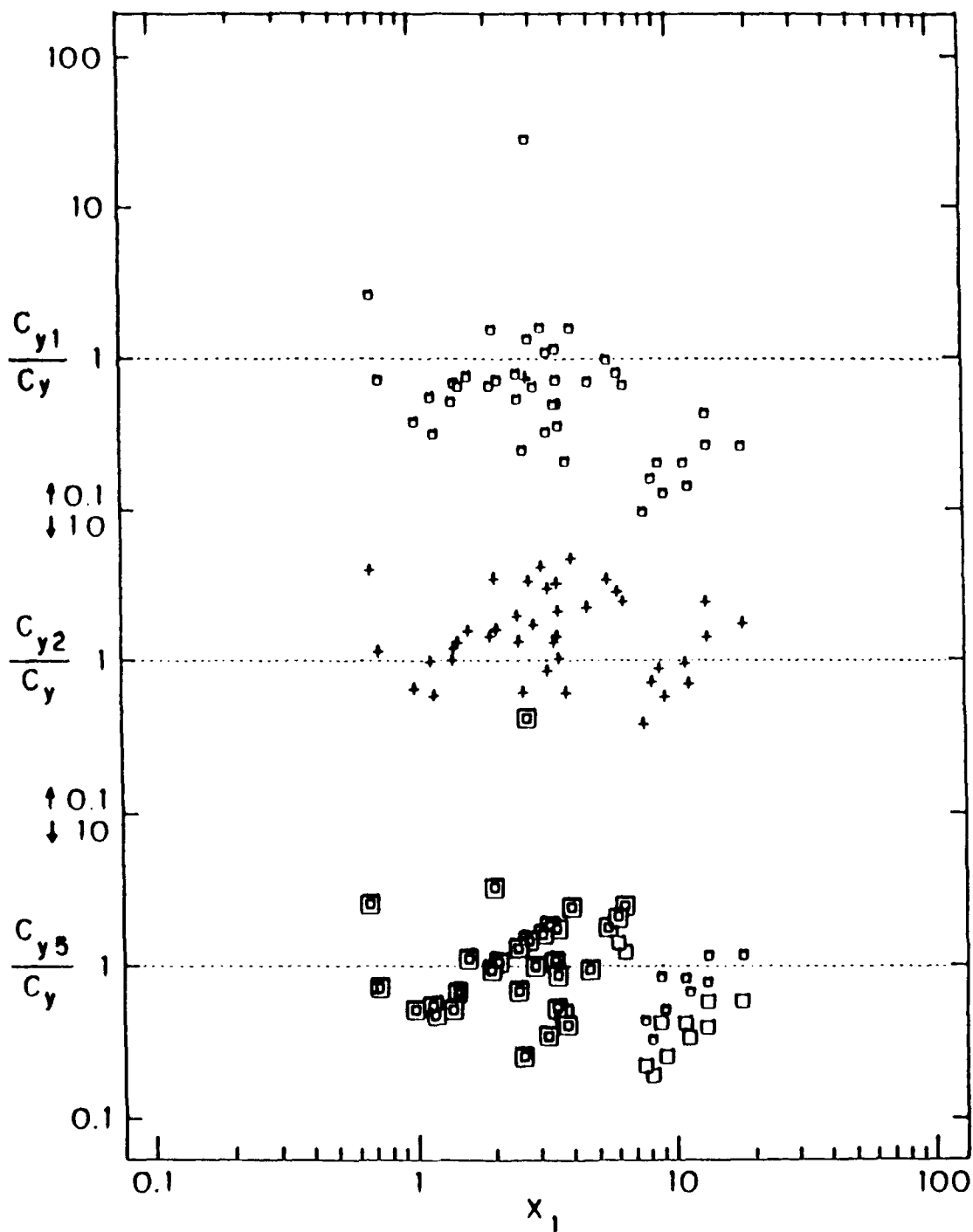


Figure 33. Ratio of predicted to measured normalized cross wind integrated concentration as a function of nondimensional distance calculated from scaling parameter measured at the source (zone 1). Models are identified in fig. 29. For model 5, small squares at $X > 6$ are model 5 predictions assuming σ_y is multiplied by a factor two.

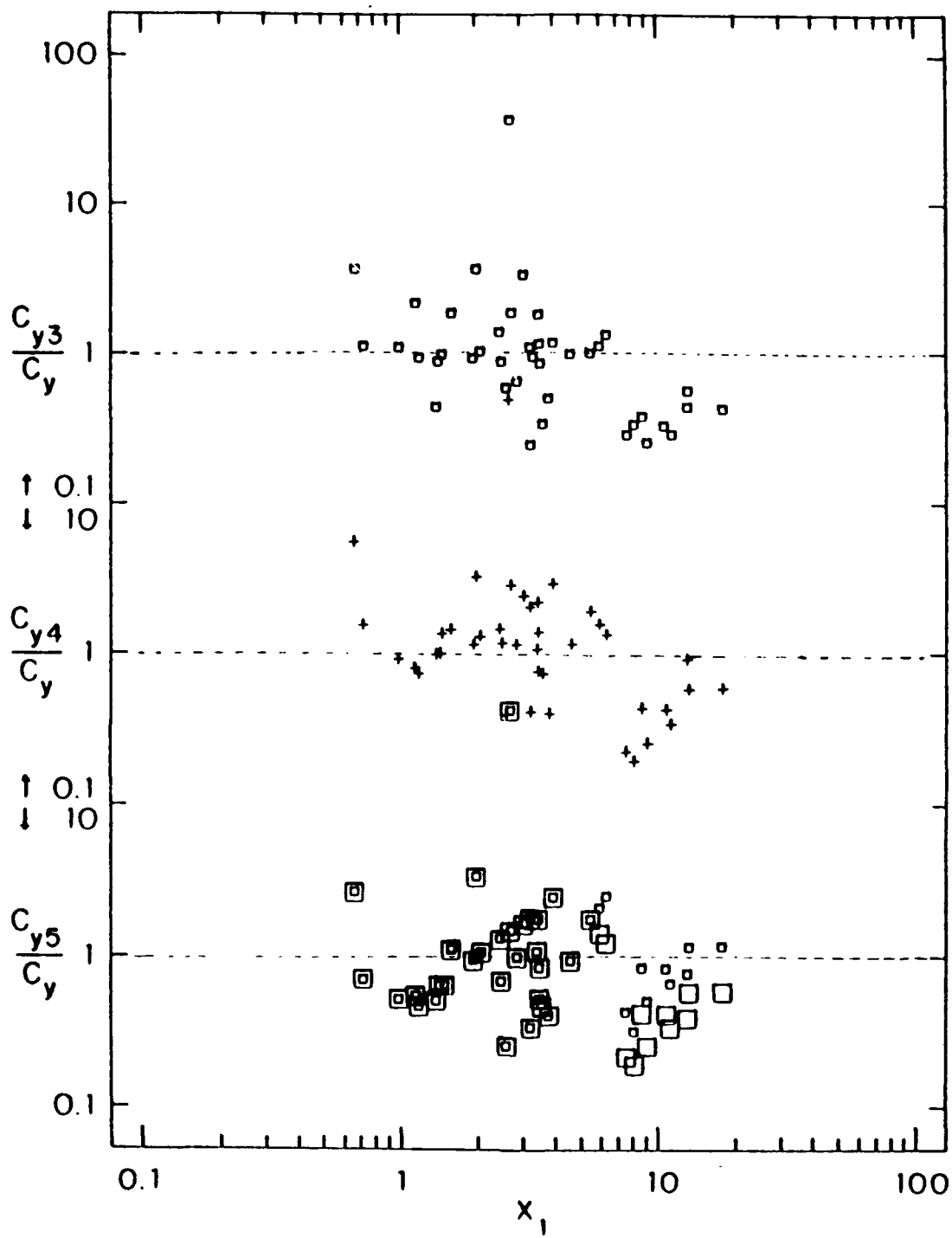


Figure 34. Same as fig. 33, except for models 3, 4, and 5.

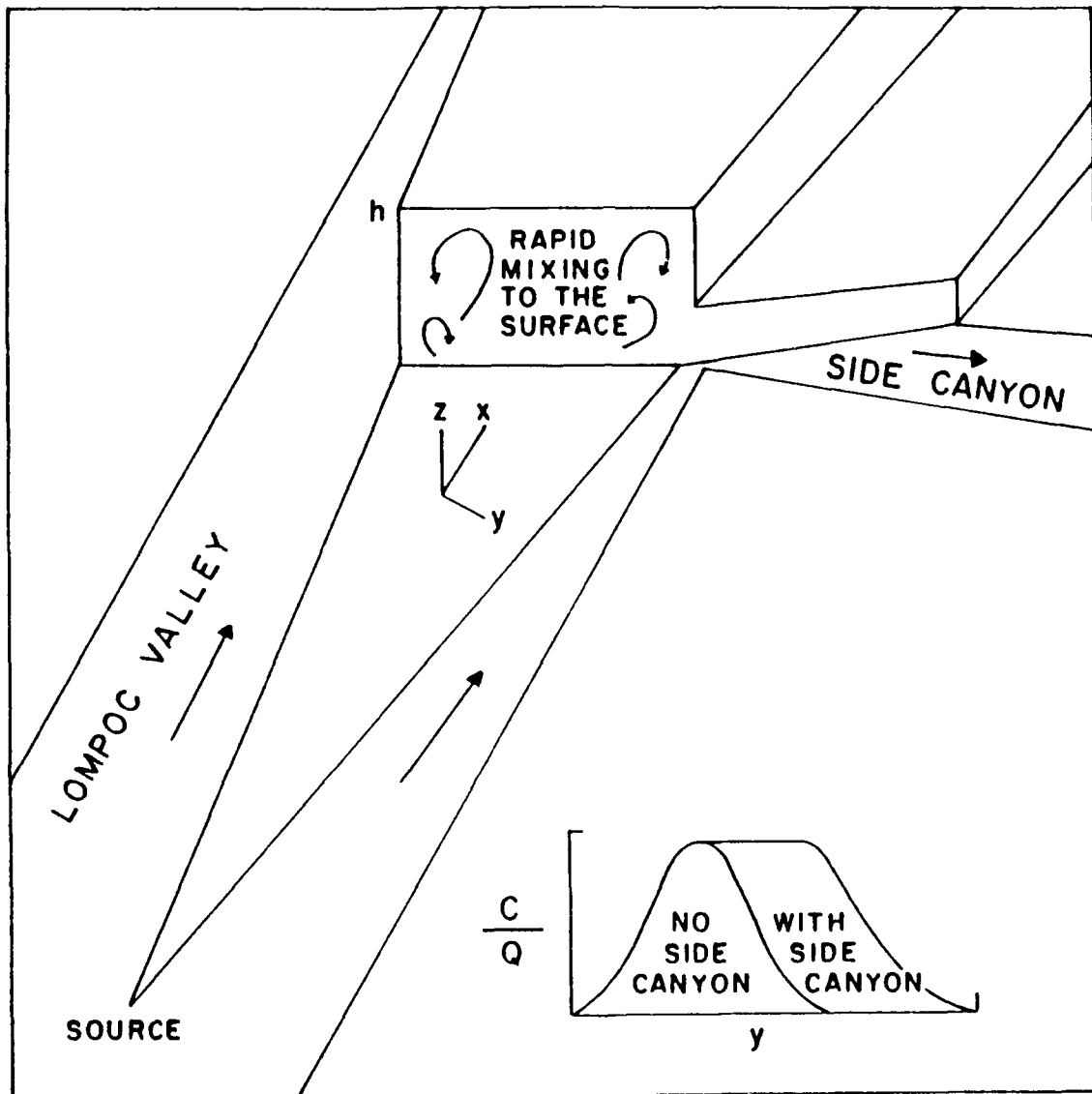


Figure 35. Schematic of topographically enhanced plume spread. Near surface wind shear is caused by ventilating effects of side canyons which intersect Lompoc Valley. Rapid vertical mixing maintains maximum concentration while enhancing surface level cross wind integrated concentration.

11. Convective Scaling Model Comparison - Statistics

Statistics were calculated for the models discussed above. Table 1 summarizes the results. All data were include in the C_0/Q statistics. Data at $X > 6$ were omitted from σ_y and C_y statistics. The general remarks of the previous section are quantified in these results. A few additional comments follow.

Table 1. Statistical Convective Scaling Model Comparison

Statistic	Mod 1	Mod 2	Mod 3	Mod 4	Mod 5
σ_y	Lower	Upper	Med.	Draxler	Two Zone
o/p ₁ average	0.72	1.80	1.33	1.17	0.99
o/p median	0.69	1.58	1.33	0.93	0.98
FB	0.44	-.50	-.17	-.03	0.10
GFB	0.59	-2.4	-3.5	-.19	0.29
q. range ₂	0.44	0.98	0.68	0.74	0.67
factor 2	0.74	0.65	0.87	0.90	0.84
factor 4	1.00	0.97	1.00	1.00	1.00
NMSE	0.46	0.64	0.21	0.21	0.29
C_0/Q					
o/p average	2.40	0.89	1.28	1.37	1.77
o/p median	1.80	0.55	1.02	1.22	1.19
FB	-.37	0.55	0.19	-.15	-.16
GFB	-.02	0.02	0.00	-.01	-.01
q. range	1.39	0.50	1.05	1.07	0.96
factor 2	0.62	0.54	0.68	0.66	0.76
factor 4	0.87	0.85	0.97	0.97	0.92
NMSE	0.51	1.15	0.48	0.43	0.43
C_y					
o/p average	1.73	4.27	3.14	2.48	2.44
o/p median	0.70	1.57	1.29	1.05	0.95
FB	0.42	-.45	-.21	0.00	0.12
GFB	0.28	****	-1.3	-.43	-.07
q. range	0.60	2.25	1.13	0.98	1.12
factor 2	0.74	0.61	0.65	0.74	0.71
factor 4	0.90	0.90	0.94	0.97	0.97
NMSE	0.74	0.69	0.44	0.35	0.49

1 o/p is the ratio of observed data to prediction

2 q. range is the interquartile range between 25 and 75% of median

Since these data are geometric (ratios), the median value is more appropriate than the average. Fractional bias (FB) is negatively correlated with the median. Model overpredictions (median > 1) are usually associated with negative FB. We see that models 4 and 5 are clearly superior in terms of median and FB, meaning they most accurately reproduce the ensemble. Geometric fractional bias (GFB) indicates trends in the bias. One can calculate significant FB with minimal GFB (e.g. C_0 predictions) or vice versa. We see large negative GFB values with modest FB for model 3 σ_y and C_y predictions. This indicates that many more data points over-predict than underpredict, even though the magnitude of that over-prediction is small.

The factor grading was explained earlier. Interquartile range (q. range) is the actual range of values corresponding to the predictions falling within a factor of two of the observations. Q. range tends to correlate with the bias, and should only be used as a measure of the relative merit of two models with equal bias. Reviewing the table, the factor grading is quite insensitive to the model quality. As discussed earlier, it is sensitive to the number of data in the ensemble. Therefore, we recommend avoiding factor grading for these type of analyses.

Normalized mean square error (NMSE) is a good measure of the scatter of data, regardless of bias. The table indicates that

models 3,4 and 5 have comparable data scatter for all quantities. Ideally, we would liked to have seen significantly reduced NMSE for the two zone model. Unfortunately, requiring cloud edge location adds degrees of freedom to the model, and likewise, scatter. This most likely offsets any scatter reduction realized with the added physics.

12. Comparison of Regressive and Convective Scaling Results

The regression analyses of sections 2-5 only predict centerline concentration. Those regressions were conducted separately for the HSSF and Lompoc Valley releases. Table 2 applies the Mt. Iron equation and the recommended time averaged regression equation (see section 5) to the full set of data. The Two Zone model results are repeated from table 1.

We see comparable statistics for the LVDE regression and Two Zone models. The Mt. Iron regression performs very poorly in terms of scatter (NMSE) and predicts a very low median value compared to the observations. A tendency towards unreasonably low predictions at greater range was discussed in the regression analysis. Oddly, the Mt. Iron fractional is negative, contrary to the lower median predictions. This is due to a few very large predictions.

The mutual agreement between the LVDE regression equation and the theoretically based two zone model further support the contention that the Mt. Iron equation should not be used for releases from HSSF. Taken at face value, we may be tempted to conclude that the LVDE regression and Two Zone model are equivalent predictors. We must realize that the LVDE regression is being compared to the very same data from which it was derived. The other two predictions are independent of the data. Given another set of data with different background conditions, the LVDE

regression could perform as poorly as the Mt. Iron regression does here. The two zone model is only confined by the physics from which it was derived, and can therefore be generalized to a wide variety of conditions.

Table 2. Convective Scaling vs. Regression Model Comparison

C ₀ /Q	regression		convective scaling
	Mt. Iron	LVDE	Two Zone
o/p average	1.33	1.50	1.77
o/p median	0.63	1.07	1.19
FB	-.25	-.04	-.16
GFB	0.02	-.01	-.01
q range	0.99	0.87	0.96
factor 2	0.36	0.75	0.76
factor 4	0.68	0.95	0.92
NMSE	2.43	0.46	0.43

13. Conclusions and Recommended Convective Scaling Equations (C_0/Q)

Application of convective scaling to LVDE reasonably agrees with the observations and theories of other investigators. Considering the partially cloud covered LVDE domain as two zones with different w_* improves the predictions. The accuracy of this formulation is comparable to statistical predictions using actual turbulence measurements and integral time scales deduced from the tracer measurements. While convective scaling predictions of centerline maximum concentration are satisfactory for all ranges, predictions of lateral plume dimension and surface level cross-wind integrated concentration fail for $X > 6$. We attribute this failure to topographic flow, namely, the ventilating effects of canyons crossing the mean plume trajectory. We speculate that centerline concentrations are not reduced because the low level nature of this up-canyon flow allows for rapid mixing of mass from the unaffected plume aloft.

We recommend using the two zone model of eqs. 31-34, when the downwind position of the cloud edge relative the source is known. This information can be obtained from satellite imagery, but errors are large and the procedure is not trivial. We recommend visual estimates. Observers with local knowledge of the terrain and landmarks should be able to locate the cloud edge with more

accuracy than satellite images. If funds become available, we also recommend that all meteorological towers be fitted with low cost photokvoltaic radiometers. Such a network would give an adequate definition of the cloud edge position. On the other hand, we recommend installation of an accurate set of short and long wave radiometers at an inland met tower for clear sky heat flux estimates. WT019, WT014, or a new tower situated in Lompoc would be good candidates. The present radiometers at WT301 should be maintained and factory calibrated periodically. These will supply adequate heat flux estimates under the clouds.

In lieu of cloud edge information, we recommend using the statistical model (eq. 17) for releases near the Lompoc Valley, during "normal" sea breeze conditions. For this purpose, we suggest using the 10 minute turbulence measurements from Building 900 (level $z = 0$ in the Building 900 DASS data file). We have already discussed the problems with using this formula at other locations or in different meteorological conditions.

For totally or partially cloud covered cases with no information on the cloud edge position, we recommend using model 1 (eq. 16), as suggested by Briggs (1985). w_* should be calculated under the stratus. This will give a conservative prediction of centerline concentration. Based on the results of this analysis, one may be tempted to use model 3 which would give lower centerline concentrations. However, we believe model 3 is most applicable to

clear sky conditions. The reasonable agreement between model 3 and the data was mainly due to the fact that the cloud edge was usually close to the source.

For totally clear skies, model 5 (two zone) reduces to model 3. Therefore, either model will produce the same results.

All of these models require boundary layer depth and wind speed input. We showed that these data are highly variable for LVDE along the plume trajectory. Since we could not unambiguously define a function of this variability, we used averaged values which produce reasonable results. This approach can be carried too far, however, if data are included in the average which are far removed from the plume trajectory. For boundary layer height, we did not include SLC6 or Building 1764 data in the average. For wind speed, we used the base average of 12 ft winds, but calibrated that average against actual boundary layer averaged wind speeds from the SODARs along the plume trajectory. We do not recommend using our calibration factor for operational purposes. Our recommendation is to use boundary layer height and average wind speed from the SODAR closest the release point. For HSSF or SLC4, that SODAR is at building 900. For north base, that SODAR is at building 1764. Boundary layer height should be interpreted from the shadowgraphs as the center of the elevated backscattered power maximum (BL2 in Skupniewicz et al. 1990, see this reference for further interpretative procedures). For wind speed, perform a

simple average of the speeds below the boundary layer height. We used a vector average, but this procedure is cumbersome and can give unreasonably low values in highly sheared conditions.

These procedures should be well suited to either a planning or emergency situation. All necessary data input should be easily acquired within a matter of minutes. The equations can be programmed into any portable computer, and results obtained with negligible run time.

14. Recommended Convective Scaling Equations (σ_y , C_y)

If the lateral plume dimensions or total ground level mass are required, one must consider the topography. The above recommendations hold for releases near the mouth of the Lompoc Valley during "normal" sea breeze conditions, provided that the downwind receptor is west of Sloans Canyon. At further distances, we cannot recommend an analytical model. When an operational numerical model becomes available, it should be tested against these data to see if the rapid plume expansion and enhanced ground level CWIC are adequately simulated.

15. Recommended Instrumentation Upgrades and Future Work

We have already made the recommendation of adding solar radiometers to the meteorological tower network to define the cloud conditions and provide radiation data for calculating surface heat flux. We additionally recommend research into application of doppler RADAR technology at Vandenberg for the purpose of defining boundary layer heights and winds. One possible candidates is "classical" doppler weather RADAR (e.g. NEXRAD). It may be possible to tap the data from one of the Vandenberg operational RADARs to produce doppler wind estimates. However, wind estimates from these low frequency, low elevation RADARs are subject to error from ground clutter, and the technique may not be feasible at Vandenberg. High frequency vertical profiling RADARs are rapidly becoming available. We recommend a model that not only profiles in the vertical, but also scans at off-zenith angles. We have emphasized the horizontal variability of boundary layer heights and winds in our research, and we feel that any expensive remote sensing research efforts or purchases at Vandenberg should address this problem.

We recommend continued development of a general numerical diffusion model for operational application at Vandenberg and other Air Force facilities. These models have a wide range of sophistication which highly correlates with "run time". For

Vandenberg, the degree of sophistication required is large. Therefore we recommend parallel development of simpler models to be used in emergency situations. For example, parts of this analysis can be applied in simple, fast, comprehensive Air Force models such as AFTOX or ADAM. Continued development of such models is critical.

Appendix A. Convective Scaling Velocity

To estimate the convective scaling velocity under clear or cloudy conditions we must know the on-site inversion base height, as well as the surface heat flux. We assume that the inversion base height is equivalent to the average height of thermal penetration, interpreted as the maximum elevated backscatter power return from the SODARs. Two elevated echo layers are sometimes observed for stratus cases, below and above the clouds. We use the center of the thin cloud top echo layer as the inversion base height. These are estimated by visually interpreting the SODAR facsimile records.

We also developed an algorithm to estimate surface heat flux from the solar and infrared sensors we had placed at these two sites. At present VBG has only one set of radiation sensors. Thus, we also included a routine to estimate downwelling solar and thermal radiation, if measured data is not available. This routine requires a fractional cloud coverage estimate as well as other

commonly available input data, such as inversion height, screen level wind speed, temperature, and relative humidity. The remainder of this section describes this routine, as well as the heat flux algorithm.

All solar radiation models require current date and time to compute sun angle, ψ . This is done in module, "SOLALT", which also computes sunrise/set times. We further modified an improvement of the simple ASHRAE model for downwelling solar direct and diffuse radiation (Iqbal, 1983) by supplying sine curve fits to seasonal adjustments for apparent extra-terrestrial radiation, atmospheric optical air mass, and column length of precipitable water. If cloud base height, z_c , and boundary layer height, h , were not available, the solar transmissivity through clouds, τ_c , was estimated, using the simple algorithm,

$$\tau_c = (1 - 0.6FCC) \quad , \quad (A.1)$$

where FCC is fractional cloud coverage of the sky. If z_c and h are available (from rawinsonde data or aircraft landing reports), the solar transmissivity for a non-reflective ground surface can be estimated more accurately from the method of Liou and Wittman (1979). This method uses sun angle and column height of precipitable water within the cloud within a bivariate polynomial regression of results taken from an accurate multi-stream discrete ordinates model. Currently, we assume that the cloud coverage is

stratiform and confined to the boundary layer, with a liquid water content of 0.78 grams/meter of cloud depth. Hence the only inputs required are date, time, cloud base height, and boundary layer depth. The algorithm can be extended easily to include other cloud types and water content. The regression form is

$$\tau_c(\mu_o, W) = \sum_{i=0}^3 \sum_{j=0}^3 b_{ij} \mu_o^i W^j, \quad (A.2)$$

where μ_o is solar zenith angle, W is precipitable water, and the b_{ij} are the coefficients obtained from the regression. For actual non-zero surface albedoes, A_s (default value, 0.15), we modify the cloud solar transmissivity, using the algorithm of Kamada (1984),

$$\tau_c = \left[\frac{1 - A_s A_c}{(1 - 0.12 A_c)(1 - 0.1 A_s)} (1 - d \phi) \tau_c + d \phi \right]^{FCC}, \quad (A.3)$$

where A_c is cloud top albedo (default value for stratiform clouds is 0.55), $d = 0.001068$, and ϕ is in degrees latitude. The total downwelling solar radiation, $SOL\downarrow$, is then

$$SOL\downarrow = (I_0 \sin(\psi) + I_{diff}) \tau_c. \quad (A.4)$$

We initiate the downwelling thermal radiation computation, using the algorithm of Martin and Berdahl (1983) which employs surface

dewpoint temperature, T_{dp} , hour of the day, Hr , and pressure, pr , to estimate the effective clear sky emissivity,

$$\epsilon_{cs} = 0.711 + 0.0056 T_{dp} + 0.00073 T_{dp}^2 + 0.013 \cos(0.262 Hr) + 0.00012 (pr - 1000) \quad . \quad (A.5)$$

T_{dp} is readily obtained from the relative humidity and temperature using standard formulas. The emissivity is then modified for clouds according to cloud base height, z_c , and fractional cloud coverage, FCC. Thus, we have

$$\epsilon_c = \epsilon_{cs} + 0.85 FCC(1 - \epsilon_{cs}) \exp(1.22 \times 10^{-4} z_c) \quad . \quad (A.6)$$

Again, boundary layer stratus clouds are assumed here but other cloud types are readily included. We compute downwelling thermal radiation by assuming the cloudy or clear sky to be a grey body thermal emitter, such that

$$IR\downarrow = \epsilon_c \sigma \theta^4 \quad , \quad (A.7)$$

where $\sigma = 5.67 \times 10^{-8}$ is the Planck black body constant. We obtain total downwelling radiation at the earth's surface by combining solar and thermal contributions via,

$$RAD\downarrow = (1 - A_s) SOL\downarrow + IR\downarrow \quad . \quad (A.8)$$

With the radiation component of the surface energy budget computed, we can obtain the atmospheric stability and temperature flux from the ground surface to the air. The Obukhov length is a measure of atmospheric stability, defined as,

$$L = -u_*^2 \theta / g k \theta_0 \quad , \quad (A.9)$$

where u_* is the surface layer friction velocity, $\theta = T(1000/p_r)^{0.285}$ is the screen height (or other height within the surface layer) potential temperature, g is gravitational acceleration, k is 0.4, the von Karman constant, and θ_0 is the Obukhov temperature scale. The temperature flux can be defined as the statistical correlation between vertical velocity and potential temperature perturbations, and is also given by

$$\overline{w' \theta'_0} = -u_* \theta_0 \quad . \quad (A.10)$$

Thus, given the downwelling radiation, we can iterate between estimates of L and estimates of surface temperature flux until both quantities converged. This requires that we compute both u_* and θ_0 . u_* comes from

$$u_* = U(z) \sqrt{\frac{k}{\ln(z/z_0) - \Psi_m}} \quad , \quad (A.11)$$

where $U(z)$ is the mean windspeed at height z , and z_0 is the surface

vegetative canopy roughness length (typically $\sim 1/7$ the mean vegetation height). We use the average value measured at the profile mast, 0.07m. We supply a new curve fit for the empirical surface layer stability function, Ψ_m , given by

$$\Psi_m = (1.19037 + 0.23 \ln(-z/L))^2, \quad (A.12)$$

which is computationally more efficient than previous algorithms. Analogous to u , θ is given by

$$\theta = \overline{\delta\theta}(z) \int \frac{k}{\ln(z/z_0) - \Psi_h} dz, \quad (A.13)$$

From Dyer and Bradley (1982), we have

$$\Psi_h = 2 \ln \left[\frac{1}{2} \left[1 - \sqrt{1 - 14 \frac{z}{L}} \right] \right]. \quad (A.14)$$

To obtain the ground surface "skin" temperature, θ_{00} , we assume that the potential temperature difference, $\theta_0 - \theta$, between the roughness height, z_0 , and height, z , is given by $\delta\theta$, and that the temperature difference, $\theta_0 - \theta_{00}$, across the laminar layer between z_0 and the surface is given by θ . This leads to the skin temperature expressed by

$$\theta_{00} = \theta - (\theta/k)(\ln(z/z_0) - \Psi_h) - \theta. \quad (A.15)$$

Since $\delta\theta$ is not known initially, θ_s is initially set to zero and θ_{00} is initially set equal to θ_s , the screen level potential temperature. They are then allowed to diverge toward equilibrium values by iteration. The net radiative budget at the surface is given by

$$\text{NETRAD} = \text{RAD}\downarrow - \epsilon_g \sigma \theta_{00}^4 \quad , \quad (\text{A.16})$$

where the ground surface emissivity, ϵ_g , has a default value of 0.95. Following the Penman-Monteith model (1948, 1965), temperature flux into the ground is estimated as, $Q_g = 0.15 \text{ NETRAD}$ with the stipulation that for stable conditions ($L > 0$), Q_g is 3.3 times larger. The Penman-Monteith equation is used to estimate the temperature flux,

$$\overline{w'\theta'_0} = \frac{-(\gamma (-\text{NETRAD} + Q_g) - \overline{w'q'_0})}{(\rho c_p (X_g s_{cc} + \gamma))} - 0.84 \overline{w'q'_0} \quad , \quad (\text{A.17})$$

where $\overline{w'q'_0}$ is the humidity flux, ρ is air density, $c_p = 1005 \text{ J kg}^{-1} \text{ K}^{-1}$ is the heat capacity of air, X_g is soil relative humidity, s_{cc} is the change rate of specific humidity with temperature for saturated air, and $\gamma = c_p/L_v \approx 0.0004^\circ \text{K}^{-1}$ is the psychrometric constant. In turn these latter parameters are obtained from standard algorithms. The Obukhov temperature scale is obtained from $\theta_s = -\overline{w'\theta'_0}/u_s$. In

this scheme, note that under neutral conditions when the temperature flux falls to zero, θ . will vanish and L becomes infinite. Thus, to avoid infinities during iterative numerical evaluation, it is better to compute the inverse Obukhov length, $1/L$.

From a rough bivariate analysis of our results, we found that a useful first guess is

$$1/L = 0.000674(300 - \text{RAD}\downarrow) \ln(10 z/z_0)/U^2(z) . \quad (\text{A.18})$$

In order to cover a wide range of radiation values, wind speeds, temperatures, and roughness lengths, the iteration procedure must be quite robust, otherwise convergence is not obtained, especially at low wind speeds. We found that the familiar Golder (1972) method was too crude to be useful. Even with a good first guess like eqn. (A.18), we found that simple iteration was unreliable, that the Newton-secant root finding procedure was needed for standard cases, and that second order Aitken acceleration was required for low wind speeds and small roughness lengths.

The Newton-secant root finding algorithm utilizes the form,

$$x_{i+1} - x_i = \delta_{i+1} = \frac{-\delta_i f(x_i)}{f(x_i) - f(x_{i-1})} , \quad (\text{A.19})$$

where i is iteration number, x here is $1/L$, and $f(x)$ is the

difference between old and new values of $1/L$. The object of the iteration process is to adjust $f(x)$ to approach zero. Unlike the standard Newton-Raphson technique, fortunately, the secant method does not require an analytic expression for the first derivative of $f(x)$ which in our case is not obtainable. The Aitken technique is a second order acceleration method found in most numerical analysis texts,

$$x_{i+3} - x_i = \delta_{i+3} = \frac{x_i x_{i+2} - x_{i+1}^2}{x_{i+2} - 2x_{i+1} + x_i}, \quad (A.20)$$

which relies on the Newton-secant method for the first two iterations then computes the rate of change of the convergence from the first two iterations and uses it to obtain a refined estimate at the third and subsequent iterations.

Once the value $1/L$ has converged, we may use it to obtain a final value for the temperature flux,

$$\overline{w'\theta'}_0 = -u_*^3 \theta / (gkL), \quad (A.21)$$

from which we can obtain,

$$\theta_* = -\overline{w'\theta'}_0 / u_*, \quad (A.22)$$

and finally the Deardorff convective scaling velocity,

$$w_* = (gh \overline{w'\theta'}_0 / \theta)^{1/3}. \quad (A.23)$$

w. has meaning only when $1/L$ is negative, i.e., the surface layer of the atmosphere is unstably stratified, such that the air above it is convectively turbulent. Turbulence intensity and hence plume diffusion scales with w^2 under such conditions. w. depends strongly on temperature flux and boundary layer height, hence, downwelling radiation and cloud cover. Thus, this series of equations suggests strong contrasts in turbulence intensity between cloud covered and clear sky zones in the coastal boundary layer.

Note however, that the convective scaling velocity is based purely on surface heating effects and inversion base height, without regard for turbulence due to wind shear. This is a good approximation for highly convective atmospheres. However, since the edge of the coastal stratus deck shifts chronically over Vandenberg, late afternoon conditions with strong seabreeze/upslope winds are typically only modestly convective and wind shear should not be ignored. In a later publication we will describe a new wind flow and turbulence model based on similarity theories extended to the outer boundary layer. Therein, we will discuss our extended turbulent scaling velocity which includes the effect of wind velocity shear at both the surface and entrainment zone.

Appendix B. Plume Centerline to Cloud Edge Determination

This section discusses the method used to determine cloud edge positions from digitized GOES-7 VAS visible light images. The cloud edge position was required to determine the distance from a given cloud edge to an SF₆ transect plume centerline position which, in turn, was needed to develop a two zone dispersion model for Vandenberg AFB.

The GOES-7 satellite was stationed at approximately 97 degrees West during the time of the LVDE experiment. Unfortunately, the GOES-West satellite stationed in the vicinity of 130 degrees West became non-operational prior to the LVDE experiment so data from a more oblique viewing angle given by GOES-7 had to be used. GOES satellites are geostationary so their orbital paths remain fairly stationary on the equatorial plane. (GOES-7 was located about two degrees south of the equatorial plane during LVDE.)

The GOES-7 optical scanning device we used was called a VISSR Atmospheric Sounder (VAS), an upgrade of the Visible and Infrared Spin Scan Radiometer (VISSR) flown on GOES - 1, 2 and 3 (Gibson, 1984). The original VISSR scanned 192 microradians per scan line in the visible region of the light spectrum - with 8 photomultiplier tubes. This gave 24 microradians per pixel in the N-S direction. The scan lines were 20% undersampled, implying that only 80% of the light within the VISSR field of view (fov) actually impinged on a

photomultiplier tube in the array. This undersampling phenomenon accounted for the discrepancy between the 21 microradian fov quoted in the GOES manual and the geometric (optimal) 24 microradian fov given by dividing the scan line width by the number of photomultiplier tubes. At any rate, the VISSR had a 25 microradian fov horizontally. 1821 scans gave a full disk view. The N-S angle of the full disk view was then:

$$1821 \times 192 \times \frac{180}{\pi} = 20.03^\circ \quad (\text{B.1})$$

The VAS also had a 192 microradian fov per scan but the N-S scan size was 24 microradians, so it did not have the undersampling problem of the original VISSR. It also had a 25 microradian E-W fov. The GOES-7 was at an altitude of approximately 35800 km so the pixel sizes were:

$$24 \times 10^{-5} \times 35800 = 0.859 \text{ km (E-W)} \quad , \quad (\text{B.2})$$

and

$$21 \times 10^{-6} \times 35800 = 0.752 \text{ km (N-S)} \quad . \quad (\text{B.3})$$

The GOES-7 VAS data was acquired from the SSEC GOES Archive at the University of Wisconsin. The data was sent on magnetic tape media

in "GARTAPE" format. There were 48 hourly images on the tape starting at 1700 and ending at 2200 hours daily between August 10 and August 17. Each of these images was examined on a video screen for image processing quality.

Next, a program was used to draw a 40 by 40 box around the domain of interest for each image and write the positions and pixel brightnesses to a data file on a floppy disk. A landmark was chosen in each image, so that the tracer source point and plume centerline positions could later be mapped accurately into this domain.

The next step in determining the distance from a cloud edge to a plume transect centerline position was to determine the pixel dimensions in the GOES images. A common method of determining pixel dimensions was to determine the change in pixel size relative to the Sub-Satellite Position (SSP) pixel dimensions using plane geometry. Several permutations of this method were tried with poor results until we found that the GARTAPE images as decoded by standard processing algorithms was distinctly non-linear and not consistent with the assumptions of plane geometry.

In the end, the pixel dimensions were determined locally on a visible image by counting the number of pixels from Pt. Conception to Pt. Sal and to Purisima Point. These distances were also measured on a fine scale map of the Vandenberg region (DMAAC, 1976). The distances and pixel counts between these landmarks were

used to determine the x and y pixel dimensions and the angle at which the GOES image was rotated relative to a local meridian. This was achieved by iterating x and y coordinate transformations with an image rotation angle to find a triad of values giving the best fit. The image rotation was found as 15 degrees (± 3 degrees) and the x and y pixel dimensions 1.0 and 1.3 km ($\pm .1$ km), respectively. We could not make this determination more accurately by taking more exact ratios over a larger domain because the non-linear distortion of the GOES image would also distort this ratio over large distances.

Once the pixel dimensions in the Vandenberg region were known a program was written to determine the distance from the cloud edge to the plume centerline (pcl) position. This required mapping the source point and pcl position onto the GOES image. Source point, pcl positions and time intervals for these two measurements were obtained from the LVDE data set and encompasses tracer transect data from three mobile gas chromatographs. A pixel counting algorithm was employed to compute the distance from the plume centerline to the cloud edge and also from the cloud edge to the source point.

For those pcl times which did not coincide with an hourly GOES image, the pcl-to-cloud edge and cloud edge-to-source point distances were time interpolated between preceding and subsequent on-hour GOES images. Since, in general, the shape of the cloud

front changed slowly from hour to hour, we made no attempt to distinguish between distance changes due to changing cloud front shape as opposed to cloud front propagation.

There were six possible sources of error in this computation:

1) determining the pixel location on the GOES satellite image which represented the location of a landmark (for instance, Pt. Conception). This error was random and was estimated as ± 1 pixel vertically and horizontally on the image.

2) determining the pixel resolution. The GOES images were scanned at an oblique angle as well as distorted by image processing. So the x and y extent of each pixel could not be determined accurately. The error in pixel resolution throughout the image was more dependent on distortion than on curvature due to oblique scanning. We estimated this error source at ± 0.2 km throughout the image by comparing pixel dimensions using 17 different landmarks. However, it was closer to ± 0.1 km over a smaller domain such as the size of Vandenberg AFB.

3) determining the cloud edge position. The appearance of clouds depended on the angle of incidence on the cloud and the dispersion of this light to the satellite sensor. Therefore, the apparent location of the cloud edge varied with these angles even though the cloud itself did not change. These errors could be partly corrected in principle, but were estimated to be small compared to

other errors. A threshold pixel brightness value (of 84 for the cloud edge) was found to be a useful value for all of the GOES images. Pixel brightness values were dimensionless and ranged from 0 to 255 for visible light images.

4) calibrating pixel brightnesses. This problem was related to the error source in 3) but was due to the VAS sensor - the VAS has no onboard calibration. No calibration was attempted and the VAS data was assumed to be calibrated in a relative sense for the duration of the experiment.

5) determining the cloud edge within a pixel. This, of course, could not be accomplished because the resolution of the image is limited to pixel dimensions. The cloud edge was therefore assumed to be at the center of the pixel which defined the edge. The percentage error in determining the pcl to cloud edge distance is therefore largest when the source, pcl and cloud edge are in close proximity. For cases in which all three of these locations are adjacent or even collocated, this error would approach the pcl to cloud edge distance itself and therefore drown out the resulting distance determinations. Since the pixels are basically rectangular, the maximum value for this error is the distance from the center of a pixel to a corner (one for the pcl pixel and one for the source pixel). For a pixel of the dimensions found in the GOES images for this experiment (1.0 km in x - direction and 1.3 km in y - direction), this comes to 0.8 km.

6) navigating the true locations of the source and plume centerline positions. The longitude and latitude of the source and plume centerline positions were estimated to be accurate to ± 0.05 minutes. This corresponds to approximately ± 0.08 km. This error is systematic for both of these measurements.

REFERENCES

- Briggs, G.A. (1985): Analytical Parameterizations of Diffusion: the Convective Boundary Layer. J. Climate Appl. Meteor., 24, 1167-1189.
- Deardorff, J.W. and G.E. Willis (1975): A Parameterization of Diffusion into the Mixed Layer. J. Appl. Meteor. 14, 1451-1458.
- DMAAC (1976): Vandenberg A.F.B. California AIM-2 Map Scale 1:62,500 Edition 2, Defense Mapping Agency Aerospace Center, St. Louis Air Force Station, Missouri 63118.
- Draxler, R.R. (1976): Determination of Atmospheric Diffusion Parameters. Atmos. Environ. 10, 99-105.
- Dyer, A.J. and E.F. Bradley (1982): An Alternative Analysis of Flux-Gradient Relationships at the 1976 ITCE. Bound. Layer Meteorol., 22, 3-19
- Gibson, J. (1984): GOES Data User's Guide - Draft Copy. National Oceanic and Atmospheric Administration, National Environmental Satellite Data and Information Service, National Climate Data Center, Satellite Data Services Division. World Weather Building Room 100, Washington, D.C. 20233.
- Golder, D. (1972): Relations among Stability Parameters in the Surface Layer. Bound. Layer Meteorol., 3, 47-58.
- Hanna, S.R. (1986): Lateral Dispersion from Tall Stacks. J. Climate Appl. Meteor., 25, 1426-1433.
- Hanna S.R. and D.G. Strimatis (1991): Uncertainties in Hazardous Gas Model Predictions. International Conference and Workshop on Modeling and Mitigating the Consequences of Accidental Releases of Hazardous Materials. American Institute of Chemical Engineers, New York, New York, 345-368.
- Hinds, W.T. and P.W. Nickola (1968): The Mountain Iron Diffusion Program: Phase I, South Vandenberg: Volume II. Air Force Western Test Range Technical Report AFWTR-TR-67-1.
- Iqbal, M. (1983): Solar Radiation, Acad. Press, NY, 1983, pps, 202 -210.
- Kamada (1984): A General Cloud Transmittance Modifier, Solar Energy Journal, 1984, p. 631

Kamada, R.F., C. E. Skupniewicz, J. W. Glendening, G. E. Schacher, T. Mikkelsen, S. T. Nielsen, I. Troen, S. Larsen, E. Takle, L. Ly, and J. Griffin (1989): Vandenberg Meteorology and Plume Dispersion Handbook for Boundary Layer Releases. Naval Postgraduate School Technical Report, NPS61-89-004, 450 pp., March 1989.

Lamb, R.G. (1979): The Effects of Release Height on Material Dispersion in the Convective Planetary Boundary Layer. 4th Symposium on Turbulence, Diffusion, and Air Pollution, Amer. Meteor. Soc., Boston, 27-33.

Lamb, R.G. (1982): Diffusion in the Convective Boundary Layer. Atmospheric Turbulence and Air Pollution Modeling, F.T.M. Nieuwstadt and H. van Dop, Eds., Reidel, 159-229.

Liou, K.N. and G.D. Wittman (1979): Parameterization of the Radiative Properties of Clouds, J. Atmos Sci., 36, 1261-1273.

Martin, M. and P. Berdahl (1983): Characteristics of Infrared Sky Radiation in the United States, LBL-16344, Lawrence Berkeley Labs.

Monteith, J.L. (1965): Evaporation and Environment. Symp. Soc. Exp. Biol., 19, 205-234.

Pasquill, F. and F.B. Smith (1983): Atmospheric Diffusion, Ellis Horwood Lim., Halstead Press, Chichester, England.

Penman, H.L. (1948): Natural Evaporation from Open Water, Bare Soil, and Grass, Proc. Roy. Soc. London, A193, 120-195

Sakiyama, S.K., and P.A. Davis (1987): Additional Field Verification of Convective Scaling for the Lateral Dispersion Parameter. J. Appl. Meteor. 27, 882.

Skupniewicz, C.E., R.F. Kamada, and L. McKay (1990): Vandenberg Boundary Layer Survey (VBLS) Final Report - Results. US Naval Postgraduate School Technical Report NPS-61-90-004, 341 pp.

Skupniewicz, C.E., R.F. Kamada, S.A. Drake, L. McKay, R.N. Abernathy, K.C. Herr, and G.J. Scherer (1991): Lompoc Valley Diffusion Experiment Data Report. US Naval Postgraduate School Technical Report NPS-PH-91-001, 150 pp.

Skupniewicz, C.E., J.W. Glendening, and R.F. Kamada (1991): Boundary Layer Transition across a Stratocumulus Cloud Edge in a Coastal Zone. Monthly Weather Rev., 119(10), 2337-2357.

Willis, G.E. and J.W. Deardorff (1981): A Laboratory Study of Dispersion from a Source in the Middle of the Convectively Mixed Layer. Atmos. Environ., 15, 109-117.

DISTRIBUTION LIST

Defense Technical Information Center Cameron Station Alexandria, VA 22314	2
Dudley Knox Library Naval Postgraduate School Monterey, CA 93943-5000	2
Dean of Research (08) Naval Postgraduate School Monterey, CA 93943-5000	1
Dept. of Physics (PH) Naval Postgraduate School Monterey, CA 93943-5000	10
Capt. D. Struck (SSD/CLGR) Los Angeles AFB Los Angeles, CA 90009-2960	5
Maj. D. Berlinrut (SSD/SEH) Los Angeles AFB Los Angeles, CA 90009-2960	1
Mr. Charles Larcomb (SSD/SDW) Los Angeles AFB Los Angeles, CA 90009-2960	1
Lt. Col. S. Pryor (30 SPW) Vandenberg AFB, CA 93437-5000	1
Maj. Anita Dye (AFSPACECOM/DOW) Peterson AFB, CO 80914-5000	1
Lt. Col. Hergenrader (AFSPACECOM/SGPB) Peterson AFB, CO 80914-5000	1
Capt. Mike Moss (AFESC/RDVS) Tyndall AFB, FL 32403-6001	1
Lt. Col. Crandall (PL/WE) Kirtland AFB, NM 87117-6008	1
Mr. Glen Boire (30 SPW/DOW) Vandenberg AFB, CA 93437-5000	1
Mr. Steve Sambol (30 SPW/DOW) Vandenberg AFB, CA 93437-5000	1

Mr. Darryl Dargitz (WSMC/SEY) Vandenberg AFB, CA 93437-5000	1
Dr. D. Ermak Lawrence Livermore National Lab P.O. Box 808, L-262 Livermore, CA 94550	1
Mr. Bruce Kunkel (PL/GPAA) Hanscom AFB, MA 01730-5000	1
Mr. Bill Boyd (45 WS/WER) Patrick AFB, FL 32925-5000	1
Mr. Dick Tatsch (45 SPW/SEMP) Patrick AFB, FL 32925-5000	1
Mr. Don Cameron (AFFTC/WE) Edwards AFB, CA 93523-5000	1
Col. Schmargie (ET) Vandenberg AFB, CA 93437-5000	1
Mr. Bob Brown US Army Atmospheric Sciences Lab SLCAS-BA-M White Sands Missile Range, NM 88002-5501	1
Mr. Ron Cionco US Army Atmospheric Sciences Lab SLCAS-AR-M White Sands Missile Range, NM 88002-5501	1
Mr. John Edwards SSD/DEV Los Angeles, AFB, CA 90009-2960	1
Mr. Randy Nyman ACTA Vandenberg AFB, CA 93437-5000	1
Larry Mendenhall Geodynamics Corp. 21171 Western Ave Suite 100 Torrence, CA 90501	1
Mr. D. Downing Geodynamics Corp. P.O. Box 5548 Vandenberg AFB, CA 93437	1

Mr. R. Hedner (Aerospace/El Segundo) PO Box 92957 Los Angeles, CA 90009	1
Dr. R. Abernathy (Aerospace/El Segundo) PO Box 92957 Los Angeles, CA 90009	1
Bart Lundblad (Aerospace/El Segundo) PO Box 92957 Los Angeles, CA 90009	1
Mr. Fred Sobottka (Aerospace/VAFB) PO Box 5068 Vandenberg AFB, CA 93437-0068	1
Mr. Lou Ullian (SE) Patrick AFB, FL 32925-5000	1
Mr. Jose Caraballo NASA Industrial Safety/RT-SOE KSC, Florida 39899	1
Mr. Jan Zysko NASA PM-PCO-4 KSC, Florida 39899	1
Dr. T. Yamada Yamada Science and Art 147 Monterey Bay Dr. S. Los Alamos, NM 87544	1
Dr. D. Pepper 5301 N. Commerce #A Moorpark, CA 93021	1
Dr. Walt Lyons 46040 Weld County Rd 13 Ft. Collins, CO 80524	1